POLITECNICO DI TORINO

Corso di Laurea in Ingegneria Aerospaziale

Tesi di Laurea Triennale

Transition to turbulence in pulsating pipe flow

Relatrice:

Prof.ssa Stefania Scarsoglio

Candidata:

Lucia Tola

Anno accademico 2023/2024

a Otto

Index

1. Introduction

The aim of this work is to study the behaviour of a pulsatile pipe flow during its transition to turbulence. In the field of fluid dynamics, a pulsatile flow is a flow characterized primarily by periodic variations. It is also known as Womersley flow, from John R. Womersley (1907-1958), a British mathematician expert in flow profiles of blood in arteries.

Examples of pulsatile pipe flow in everyday life are found in many fields, such as in the cardiovascular system, in industrial pumps, in engine coolant systems and in microfluidic devices. From this wide range of applications, it is therefore possible to understand the importance of studying this type of flow and understanding its characteristics, especially for what concerns the transition to turbulence. The knowledge of this specific topic is still particularly debated, as there is little consensus regarding the influence of some factors, e.g. the pulsation, on the transition threshold to turbulence.

The first chapter of this work is meant to provide basic knowledge of the pulsatile pipe flow, thus considering some dimensionless parameters, i.e. the Reynolds, Womersley and Strouhal numbers, and the fluid dynamics equations that describe pipe flows.

The second chapter is focused on the transition to turbulence of the flow in a rectilinear, cylindrical and smooth pipe. This part also considers instabilities and the different turbulence structures that may take place. A wide range of experiments support the theoretical dissertation, which in the end examines different aspects of the transition, e.g. transport phenomena, time related aspects and effects of waveform.

The third chapter takes into account different configurations of the pipe, that vary from the ideal case. The first one considers a constriction in the pipe; then a change in curvature is analysed, followed by the compliant walls case; the last aspect that is examined is the effect of roughness. This entire part is discussed in parallel with the blood flow model and cardiovascular system applications.

2. Basics of pulsatile pipe flow

There are several dimensionless parameters that govern the pulsatile flow behaviour, among which the most useful are: the Reynolds number, the Womersley number and the Strouhal number, which are exposed right below. After these, the equations that describe pipe flows are reported.

2.1 Reynolds number

The Reynolds number is an essential dimensionless parameter, helpful for the analysis of pulsatile flows, derived from the Navier Stokes equations. As it expresses the ratio of inertial forces to viscous forces, it is used to predict the onset of turbulence in fluid flow. Considering the axial velocity u, in the case of pulsatile flow it is generally composed by two components: the steady velocity component u_s and the oscillatory component u_o. It is thus possible to define two parameters related to each velocity,

the mean Reynolds number:

$$Re_m = \frac{2u_s R}{v}$$

and the oscillatory Reynolds number:

$$Re_o = \frac{2u_o R}{v}$$

where R is the radius of the pipe and ν the kinematic viscosity. For what concerns a fluid flow in a pipe, if $Re < 2300$ the flow is laminar, whereas if $Re > 2300$ the flow is generally considered turbulent.

It is also frequent to use the ratio Re_o/Re_m, as it describes the ratio of oscillating and mean velocity component.

2.2 Womersley number

The Womersley number is defined by the following equation:

$$\alpha \equiv Wo = R\sqrt{\frac{\omega}{\nu}} = R\sqrt{\frac{\omega\rho}{\mu}}$$

Where R is an appropriate length scale (e.g. the radius of the pipe), ν the kinematic viscosity (remembering that $\nu = \frac{\mu}{\rho}$, with μ dynamic viscosity, ρ density) and ω the angular velocity of the oscillations which is tightly related to the frequency of oscillation ($\omega = 2\pi f$). The Womersley number is a biofluid mechanics and dynamics parameter that expresses the relationship between the pulsatile flow frequency and the viscous effects, giving the ratio of transient inertial forces to viscous forces. The Womersley number arises in the solution of the linearized Navier Stokes equations for oscillatory flow (laminar and incompressible) in a tube.

When α is smaller than 1, the frequency of pulsations is sufficiently low that a parabolic velocity profile develops during each cycle: the flow is almost in phase with the pressure gradient and the Poiseuille's law would be a good approximation. For larger values of α, the velocity profile is relatively flat, and the mean flow lags the pressure gradient by about 90 degrees. The Womersley Number is therefore important in studying dynamic similarity when scaling an experiment.

A bond between these two key parameters exists, as they are linked by the following equation, that involves the Strouhal number as well, which is discussed hereafter: $\alpha = \sqrt{2 * \pi * Re * St}$.

2.3 Strouhal number

The third dimensionless parameter is the Strouhal number, used to describe oscillating flow behaviour. It represents the ratio of inertial forces due to local acceleration of the flow to the inertial forces due to convective acceleration. In periodic flows, the Strouhal number is associated with the flow's oscillations due to the inertial forces relative to the velocity changes due to convective acceleration of the flow field. It is defined as:

$$St = \frac{fL}{v}$$

where f is the frequency of oscillation, L is the characteristic length (e.g. diameter of the pipe) and v is the velocity of the flow.

Intermediate-high Strouhal numbers (St ≥1) mean that the flow is dominated by the oscillations, often associated with vortex shedding, while at low Strouhal numbers (St<<1) the fast moving fluid sweeps away the oscillations and the flow has basically a steady behaviour.

2.4 Pipe flow equations and characteristics

The Navier-Stokes equations for an incompressible fluid with constant properties in cylindrical coordinates are written as it follows:

$$\frac{\partial v_r}{\partial r} + \frac{v_r}{r} + \frac{1}{r}\frac{\partial v_\theta}{\partial \theta} + \frac{\partial v_z}{\partial z} = 0\,, \tag{1}$$

$$\frac{\partial v_r}{\partial t} + v_r\frac{\partial v_r}{\partial r} + \frac{v_\theta}{r}\frac{\partial v_r}{\partial \theta} + v_z\frac{\partial v_r}{\partial z} - \frac{v_\theta^2}{r} = -\frac{1}{\rho}\frac{\partial p}{\partial r} + \nu\left(\nabla^2 v_r - \frac{v_r}{r^2} - \frac{2}{r^2}\frac{\partial v_\theta}{\partial \theta}\right), \tag{2}$$

$$\frac{\partial v_\theta}{\partial t} + v_r\frac{\partial v_\theta}{\partial r} + \frac{v_\theta}{r}\frac{\partial v_\theta}{\partial \theta} + v_z\frac{\partial v_\theta}{\partial z} + \frac{v_r v_\theta}{r} = -\frac{1}{\rho r}\frac{\partial p}{\partial \theta} + \nu\left(\nabla^2 v_\theta + \frac{2}{r}\frac{\partial v_r}{\partial \theta} - \frac{v_\theta}{r^2}\right), \tag{3}$$

$$\frac{\partial v_z}{\partial t} + v_r\frac{\partial v_z}{\partial r} + \frac{v_\theta}{r}\frac{\partial v_z}{\partial \theta} + v_z\frac{\partial v_z}{\partial z} = -\frac{1}{\rho}\frac{\partial p}{\partial z} + \nu\nabla^2 v_z\,, \tag{4}$$

considering:

$$\mathbf{v} = v_r\mathbf{e}_r + v_\theta\mathbf{e}_\theta + v_z\mathbf{e}_s$$

and where:

$$\nabla^2 = \frac{1}{r}\frac{\partial}{\partial r}\left(r\frac{\partial}{\partial r}\right) + \frac{1}{r^2}\frac{\partial^2}{\partial\theta^2} + \frac{\partial^2}{\partial z^2}\,.$$

The case of an infinite straight conduit with circular section and constant diameter is a case of parallel flow. Using cylindrical coordinates, with the axis z corresponding to the conduit axis, the solution will be in the following form, because of the axial symmetry:

$$\mathbf{V} = \{0,0,u(r)\}$$

with boundary condition $u(R) = 0$, with R is radius of the circular section. Consider also that the pressure has a dependence on the z coordinate (p=p(z)).

With such boundary conditions, the continuity equation (1) is automatically satisfied, as well as the components of the momentum equation along r and theta. The equation (4) will become:

$$\mu\left(\frac{d^2u}{dr^2} + \frac{1}{r}\frac{du}{dr}\right) = \frac{dp}{dz},$$

Since the left term depends on r, and the right term depends on z, the equation is satisfied only if both terms are constant and equals, so:

$$\frac{dp}{dz} = -G \implies \mu\left(\frac{d^2u}{dr^2} + \frac{1}{r}\frac{du}{dr}\right) = -G\,.$$

From the first one we obtain that $p(z) = C - Gz$, whereas the second one can be rewritten as:

$$\frac{d}{dr}\left(r\frac{du}{dr}\right) = -\frac{G}{\mu}r\,,$$

integrating it we obtain:

$$\frac{du}{dr} = -\frac{G}{2\mu}r + \frac{C_1}{r} \implies u(r) - \frac{G}{4\mu}r^2 + C_1\ln r + C_2$$

In order to have a finite value of the velocity for $r = 0$ we have that $C_1 = 0$, and from the initial boundary condition we obtain:

$$u(r) = \frac{G}{4\mu}R^2\left(1 - \frac{r^2}{R^2}\right)$$

As $G = -dp/dz$, the velocity profile of the pipe flow in an infinite straight conduit with circular section and constant diameter, better known as Hagen-Poiseuille flow, is:

$$u(r) = -\frac{R^2}{4\mu}\frac{dp}{dz}\left(1 - \frac{r^2}{R^2}\right).$$

The velocity profile has the shape of a paraboloid, with maximal velocity at the centre of the pipe (Figure 1).

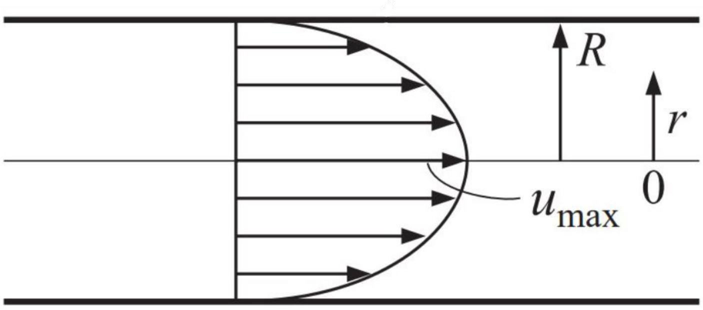

Figure 1: Hagen-Poiseuille flow velocity profile 2D [18]

This solution works effectively as long as the speed is restrained: being the other parameters equal, in particular, the corresponding Reynolds number have to be lower than $Re_{crit} = 2300$. For higher values, this solution is no longer valid, as the flow is characterized by turbulence. [18]

3. Transition of pulsatile flow in straight pipe configuration

Most fluid flows in nature and in everyday applications are subject to periodic velocity modulations. However, the consensus regarding the influence of pulsation on the transition threshold to turbulence is little: some studies predict a monotonic increase of the threshold with the frequency (i.e. Womersley number), others report a decreasing threshold for identical parameters and only observe an increasing threshold at low Wo. It is then clear why the mechanisms of transition of pulsatile flow are still under investigation and debate.

Pulsatile flows are often at the verge of being turbulent, as cardiovascular flow confirms, with Reynolds numbers in the larger blood vessels in transitional regime. These turbulent fluctuations have been associated with a wide range of cardiovascular diseases. But, as non-Newtonian fluids, the physiological fluids are more complicated to study and fully understand, also because of their complex geometry that causes additional complications. Nevertheless, also the simplest case of transition in pulsatile flow of a Newtonian fluid in a straight pipe is not well understood. Where steady pipe flows are governed by the only Reynolds number, for pulsating flows it is necessary to consider all the followings: Reynolds number Re_m, the ratio $A = Re_o/Re_m = u_o/u_s$ and the pulsation frequency, generally expressed by the Womersley number. [1]

Before analysing the transition to turbulence, the following equation is needed:

$$u(r,t) = \frac{p_s}{4\mu}(r^2 - R^2) + \frac{p_o R^2}{i\mu\alpha^2}\left\{1 - \frac{J_o(\alpha \frac{r}{R} i^{\frac{3}{2}})}{J_o(\alpha i^{\frac{3}{2}})}\right\} e^{i\omega t} \tag{5}$$

It describes the axial velocity u as function of radial position r and time t (figure 2). It is valid for an axisymmetric flow of an isotropic, incompressible, Newtonian fluid without external forces. In the equation, p_s is the time independent pressure gradient, $p_o e^{i\omega t}$ the time dependent pressure gradient. The first term is basically the classic parabolic Poiseuille flow, whereas the second one represents the effects of transient inertia, with J_o a Bessel function. [2]

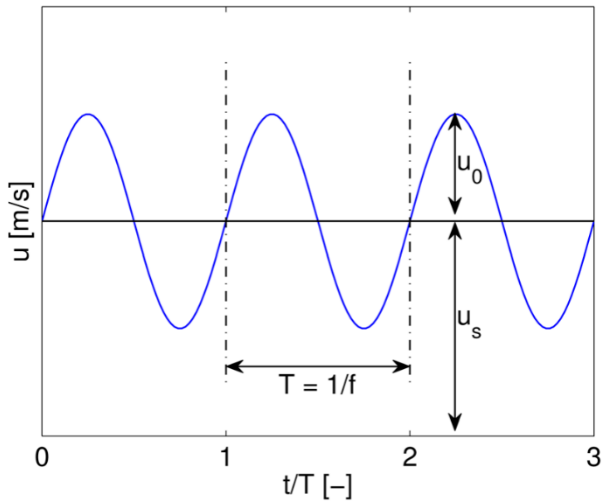

Figure 2: The sinusoidal axial velocity u and the definition of the mean velocity, the oscillatory velocity, the frequency, and the period T [2]

3.1 Laminar flow

Considering the measurements conducted by Trip et al [2] for both steady and unsteady flow, the range of mean Reynolds number considered is the one for which transition is expected ($Re_m = 2000 \div 3500$). As the data has a consistent convergence for fifty recordings, that number will be considered as sufficient for the experiments, as shown in figure 3.

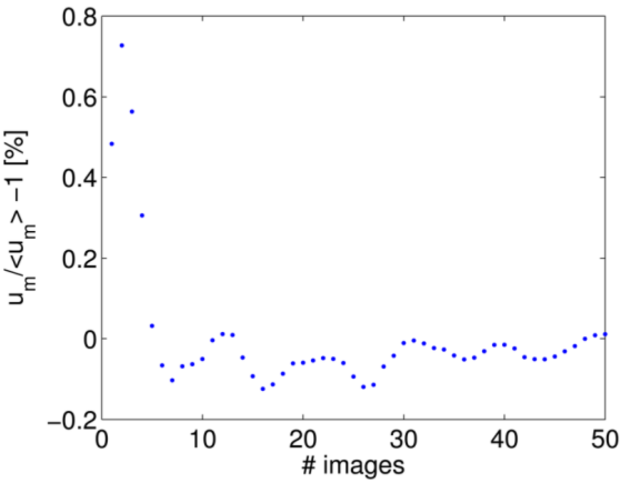

Figure 3: The mean velocity as function of the number of images used [2]

It is a reason of interest to compare the velocity profiles of laminar steady, oscillatory, and pulsatile flow with the theoretical shape. An example of these instantaneous profiles is given by figure 4, where the mean component (x), the oscillating component (.) and their sum (o, 'pulsatile') are shown for both laminar and turbulent case. For the laminar case, the continuous lines indicate the theoretical behaviour derived from the equation (5).

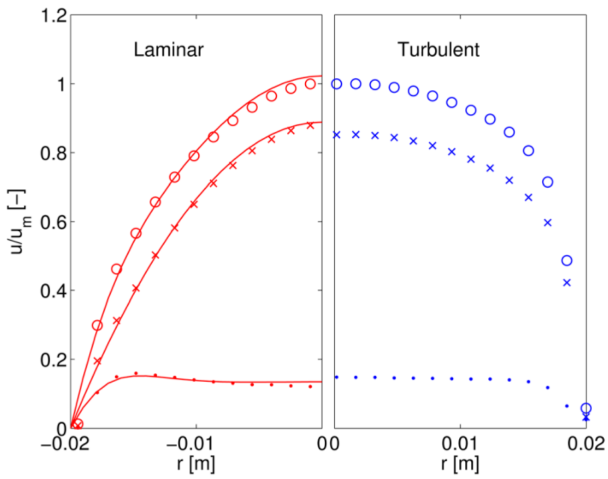

Figure 4: Left: Measured and theoretical steady u_s (x), oscillatory u_o (.) and pulsatile u_m (o) velocity profiles of a laminar pulsatile flow (α=10, Re_m=2160 and Re_o=610). Right: Measured steady u_s (x), oscillatory u_o (.) and pulsatile u_m (o) velocity profiles of a turbulent pulsatile flow (α=10, Re_m=3160 and Re_o=610) [2]

Notice that for the turbulence case, the velocity distribution is more uniform as a result of more efficient momentum transport due to eddies. [2]

3.2 Transition of steady flow

According to Trip et al studies [2], the transition of steady flow is examined first. The turbulence intensity is measured for a range of mean Reynolds number from 2000 up to 3500 and it is again the statistical average over fifty realizations. Considering the volumetric flow rate controlled, the mean Reynolds number is corrected for the temperature dependence of the kinematic viscosity.

Figure 5 shows the turbulence intensity based on the radial and axial velocity. The error bars denote the standard error of the mean. For the axial component, a large overshoot at $Re_m = 2388$ is marked.

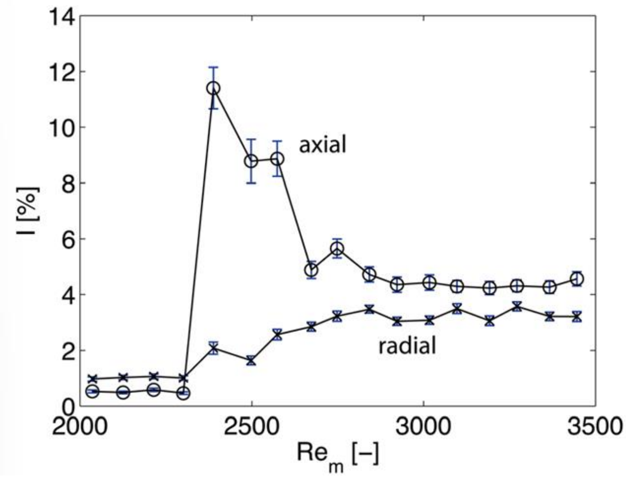

Figure 5: Normalized intensity of turbulence at the centreline. Axial (O) and radial (X) components are shown separately [2]

The mean velocity component of turbulent flows appears to be smaller than laminar flows, because of the better efficiency in the momentum transfer. The intermittent nature of the transitional regime leads to having the ensemble average of the mean velocity biased and it results with the increase of the velocity fluctuations. It is to be noticed that the overshoot does not have a clear value for the intermittency. To avoid it a solution would be looking at the radial velocity component, for which the mean component is equal to zero for both the laminar and turbulent flow state. For this reason, the only radial component of the velocity is used to study the transition to turbulence in this chapter.

Up to $Re_m \approx 2400$, the normalized intensity of turbulence is around 1%. The flow is still considered laminar, and this little turbulence intensity is mainly due to measurements errors and small fluctuations in the pump output. In the so-called transitional regime ($Re_m \approx 2400 - 2800$) the turbulence intensity rises: in this region, puffs occur randomly and increasingly in time. For $Re_m > 2800$, the turbulence intensity is approximately 3%. [2]

Note that the turbulence intensity is defined as follows:

$$I = \frac{1}{u}\sqrt{\frac{1}{3}(\langle u'^2\rangle + \langle v'^2\rangle + \langle w'^2\rangle)} \tag{6}$$

Where u is a reference velocity and u', v', w' are the turbulent fluctuations of the velocity and are function of the axial, radial and azimuthal position.

3.3 Transition of unsteady flow

Because of the intermittent nature of the flow, a direct calculation of the turbulence intensity is not representative of the reality. A possible approach is to subtract the line average in the axial direction for each fluctuating velocity field:

$$\Psi'_{mod,i}(x,r) = \Psi'_i(x,r) - \frac{1}{L}\int \Psi'_i(x,r)\, dx\,. \tag{7}$$

This solution is only possible if the turbulent structures (i.e. puffs) have a comparable size with the width of the field of view, condition that in general is fulfilled. Considering typical puffs dimension, the error connected to this aspect is very small. Subtracting the line average allows to correct the velocity fluctuations as well as the pump fluctuations.

In Trip et al. [2] studies the measurements for the unsteady flow case are conducted over a range of mean Re numbers Re_m for a single velocity amplitude (i.e. $Re_o \approx 610$) and four different Womersley numbers ($\alpha \approx 10 - 25$). The measurements of their studies are reported in table 1 and figure 6.

α [−]	f [1/s]	f_t [1/s]	T_t [s]	u'/D [1/s]
0	0.0000	1.000	50	0.0775
10	0.0398	0.318	1256	0.0900
15	0.0895	0.716	559	0.0692
20	0.1592	1.273	314	0.0825
25	0.2487	1.989	201	0.0955

Table 1: Measurements of unsteady pulsatile flow, f is the frequency of pulsation, Tt is the frequency of the measurements, u'/D is an estimate of the reciprocal value of the turbulence integral timescale [2]

From figure 6 it is evident that no clear differences can be observed for the different pulsatile flows, reason why a single fit is plotted. This confirms that the influence of pulsation is limited to Womersley numbers below 10, as reported by Stettler and Hussain [4]. The intensity graph has a s-like shape, which resembles the graph of the intermittency as a function of Reynolds number, reported as well by Yellin [5] with flow visualization. This seems to confirm the idea [2] that the increase in puff number causes the smooth increase in turbulent intensity.

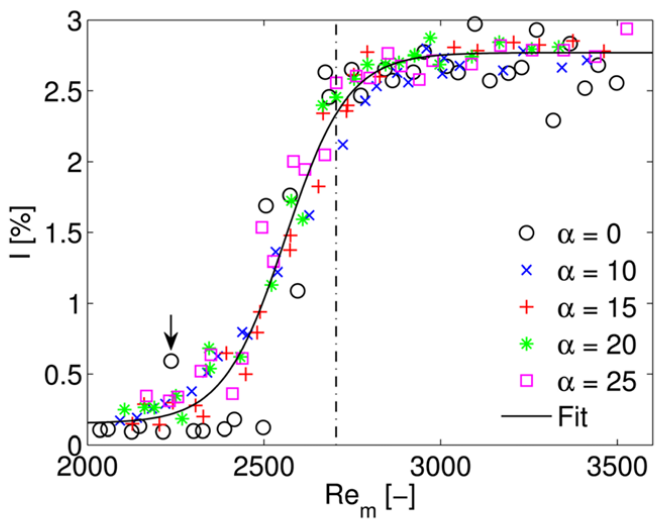

Figure 6: Turbulence intensity at centreline as function of mean Re for five different Womersley numbers [2]

Within the transitional range of Reynolds number, the influence of different values of Re_m on the turbulence intensity is analysed (figure 7). A single spike in the turbulence intensity is observed for $Re_m = 2232$ at $t/T \approx 8$, whereas for the rest of the observation the intensity is zero (laminar flow). Increasing the mean Reynolds number, the number of spikes increases along with the persistence in time of the turbulence intensity. At $Re_m = 2761$ the intensity is around 3% for the entire observation (fully developed turbulent flow).

The observed spikes are due to inlet conditions and indicate the presence of a turbulent puff. From table 1 it is evident that a puff is captured in more instantaneous velocity fields for higher Womersley numbers. Differently from the steady case, for the unsteady cases the total measurement time is longer than the survival time of the individual puff. [2]

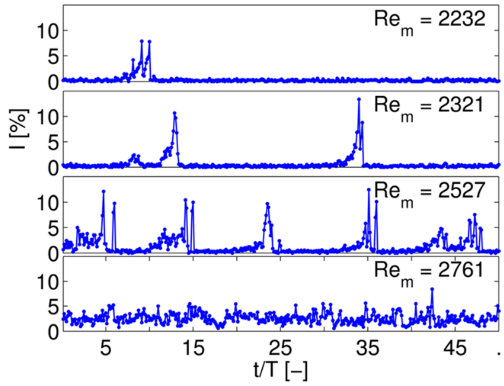

Figure 7: Turbulence intensity as function of t/T for four different mean Re, oscillatory Re of 610 and Womersley number of 25 [2]

The presence of puffs is confirmed by visualization using Iriodin flakes (figure 8). For both steady and unsteady transitional flow, a series of images is recorded with 10 Hz of frame rate, with the aim of capturing the passage of a puff. For both cases, the typical structure of a puff is recognizable in figure 8: conical tail of turbulence at the centreline downstream side of the puff and initial turbulence at the wall at the upstream side.

The figure allows some considerations on velocity fluctuations in radial direction as well (measured with PIV). The velocity data appears to show a smaller puff, but this is caused by large velocity fluctuations in the core of the puff, compared to the ones in its downstream tail. [2]

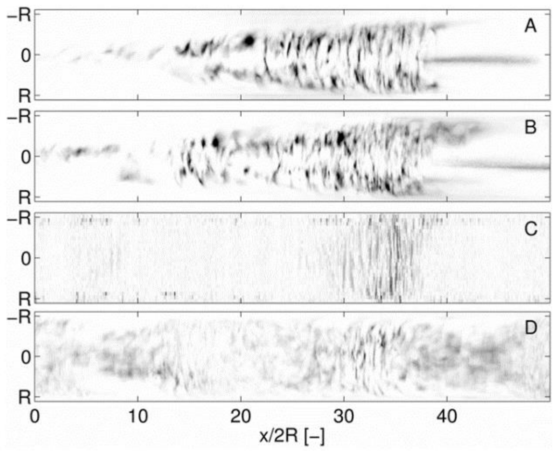

Figure 8: Visualization of a puff for unsteady (A) and steady (B) flows. Velocity fluctuations in radial direction (C). Phase-locked regime (D). Flow direction is from right to left. Horizontal axis is compressed in relation to vertical axis [2]

Considering a fixed mean Reynolds number $Re_m \approx 2700$, the influence of oscillatory Reynolds number is analysed (figure 9). Apparently, the turbulence intensity increases with Re_o, but it must be considered the fact that the temperature was not constant during the measurements, leading to a slight increase in Re_m. This causes the increase in intensity.

Therefore, the turbulence intensity is not a function of the oscillating Reynolds number, which suggests that the transition behaviour is not influenced by it as well. [2]

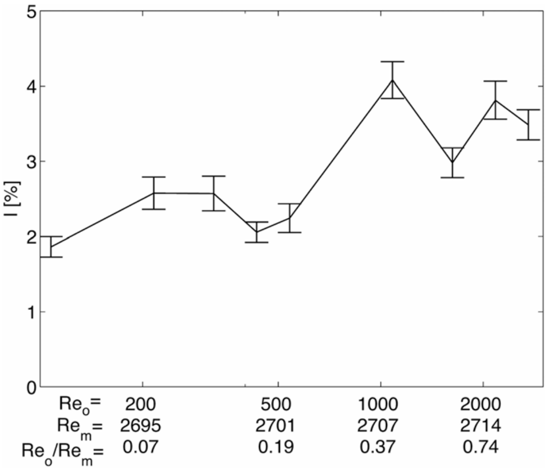

Figure 9: Turbulence intensity as a function of oscillatory Reynolds number [2]

3.4 Phase-Locked turbulence

Always according to Trip and al. [2] work, the phase-locked turbulence is a completely different phenomenon from the random occurrence of puffs. A good explanation of this event is that the entire flow bursts into turbulence and then partially relaminarizes. The parameters of the two measurements are reported in table 2. In general, up to a Womersley number of 25, phase-locked turbulence is expected for mean Reynolds above 2700 and oscillatory Reynolds above 1400.

Re_m [−]	Re_o [−]	Re_o/Re_m [−]	α [−]	f [1/s]	f_t [1/s]	u'/D [1/s]
4000	1610	0.40	15	0.0895	3.580	0.1000
5000	4000	0.80	20	0.1592	3.184	0.1350

Table 2: Measurements of unsteady pulsatile flow [2]

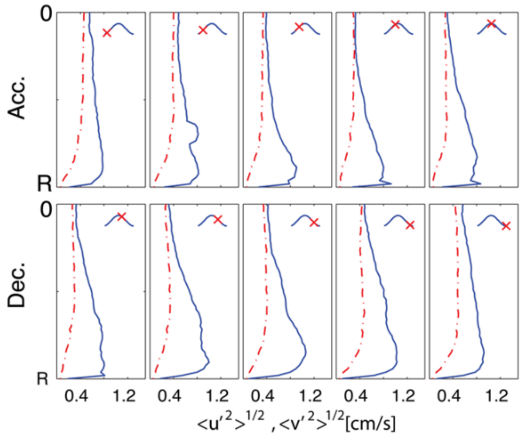

Figure 10: u' and v' as function of time over the radial position r (R pipe radius), Rem=4000, Reo=1610, Wo=15 [2]

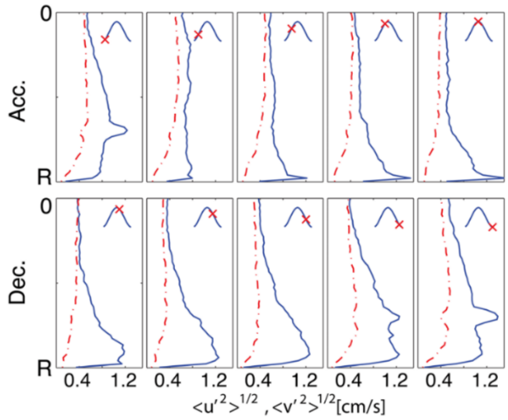

Figure 11: u' and v' as function of time over the radial position r (R pipe radius), Rem=5000, Reo=4000, Wo=20 [2]

To understand the occurrence of turbulence of the phase of pulsatile flow, a look at turbulence characteristics over the pipe radius as function of phase is needed (figure 10 and 11).

For both cases a small bump is shown around r=3/4R, caused by reflection of light in the raw PIV images and that can be slightly reduced with image background reduction. The magnitude of the turbulence fluctuations near the centre is comparable. Near the wall it starts to increase at maximum acceleration: this increase continues until maximum deceleration is reached. This is consistent with the concept of transport and is also observed for radial component, which increases as the axial velocity fluctuations increase towards the centre.

For the intensity of the entire pipe, the turbulence intensity is integrated over R, the pipe radius. What is observed is that the intensity decreases during the accelerating phase and increases during the deceleration (figure 12 and 13). Just before the deceleration stops, a maximum is reached and is then followed by a constant phase. Both cases confirm that the turbulence intensity maintains the same phase lag of the velocity. Reasons behind this behaviour might be that during deceleration the flow has inflection points in the velocity profiles, condition that probably leads to unstable flow.

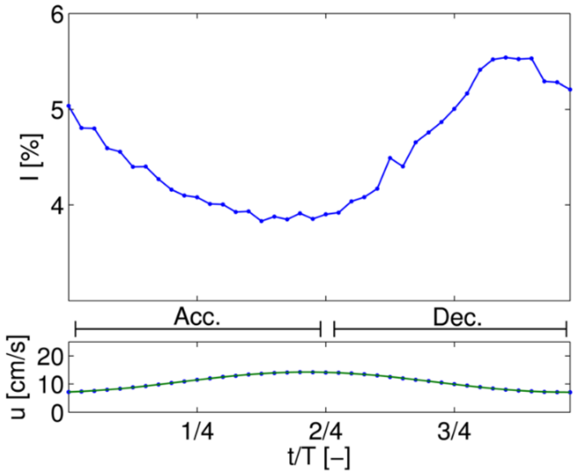

Figure 12: Turbulence intensity as function of time for Rem=4000, Reo=1610, Wo=15 [2]

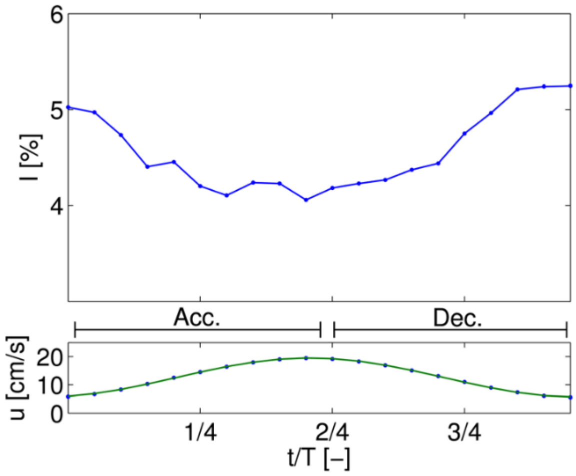

Figure 13: Turbulence intensity as function of time for Rem=5000, Reo=4000, Wo=20 [2]

The possibility of relaminarization during the acceleration probably depends on the oscillating frequency, since it takes some time for turbulence to decay. For the cases examined here, the flow does not completely relaminarize. This can be explained by the turbulence integral timescale, which is of the same order of magnitude as the frequency of the pulsation (table 2). Simply stated, there is not enough time for turbulence to decay completely.

3.5 Transition to turbulence experiments

In this section the experiments concerning transition to turbulence and puffs survival lifetime, conducted by Xu et al. [1], are reported. The experiments were carried out in straight rigid pipes with a circular cross section. The various set-ups differed in the pipe diameter and length. Defining the measurement length as the distance between the perturbation and the measurement point, so without considering the entrance length, there are three different set-ups.

3.5.1 Experiments set-ups

The first one is composed of five glass tubes for a total length of 5.5 m, with inner diameter of D=10±0.01 mm. The dimensionless length is thus 550D (actual measurement length is 330D). The second set-up involves acrylic tubes with inner diameter of D=7.18±0.02 mm and measurement length of 1300D. For the third case the pipes are again glass made (D=4±0.01mm) with the measurement length of 2250D. For all these cases, the various segments that formed the pipe were carefully aligned and a seamless fit was guaranteed.

The pipe is connected to a reservoir via a trumpet-shaped convergence section (figure 14). The end of the pipe is connected to a Pneumax piston, 1.2 m long with a diameter of 40 mm, pulling the water through the pipe. The piston is connected to a linear traverse (HepcoMotion PSD120) moved by a stepper motor (Dunkermotoren BG65PI).

The piston speed was controlled via a PC and was sinusoidally modulated to produce a pulsating

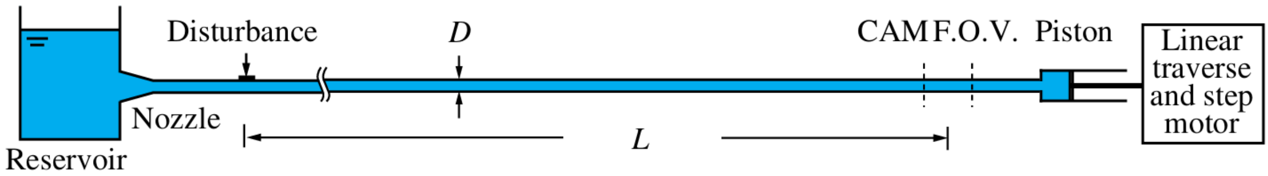

Figure 14: Sketch of the experiments set-up [1]

flow. For the entire parameter regime under investigation the pipe flow was laminar unless being disturbed. The quality of the pipe facility was tested carrying out some PIV (particle image velocimetry) measurements for a pulsating flow at Reynolds number of 2000, Womersley number of 5, amplitude of 0.4 and absence of perturbation; these tests were in fully agreement with analytical predictions for laminar pulsating pipe flow. To create disturbances, a brief injection of fluid through a 1 mm hole in the pipe wall is needed. The ratio of the injection and pipe flow is around 2%, that allows the generation of a single puff at the injection point.
To obtain a single puff (general length of 20D), the duration of injection is adjusted depending on the Womersley number to cover a specific phase of the sinusoidal motion. It was observed that variations in the phase of the injection turned out to have almost no effect on the transition threshold. On the other hand, the injection duration is relevant as long durations lead to multiple puffs.
For visualization purposes, the water contained particles (fishsilver) and a light sheet and a camera were positioned at a distance L downstream from the perturbation point. The resulting images allow to distinguish immediately between laminar and turbulent flows (figure 15). Puffs as well are readily detectable by a change in the average grey scale level or by monitoring spatial fluctuations.

Figure 15: Flow visualization images for laminar and turbulent flows [1]

3.5.2 Results and discussion

The parameters ranges used to perform the experiments are the following: Womersley numbers $1.5 \leq \alpha \leq 22$, amplitudes $0 \leq A \leq 0.7$ and Reynolds numbers $Re < 3500$ (the Reynolds numbers are calculated considering the steady component of the velocity). The flows appear laminar as long as they are not disturbed (figure 16a), but localized patches of turbulences can be detected for large enough Re (figure 16b). For fixed combinations of (α, A), the Reynolds number was varied to find a regime with strong perturbations enough to result in turbulent puffys. The probability of puffs survival over a fixed distance was then determined, as a function of Re. For individual puffs the

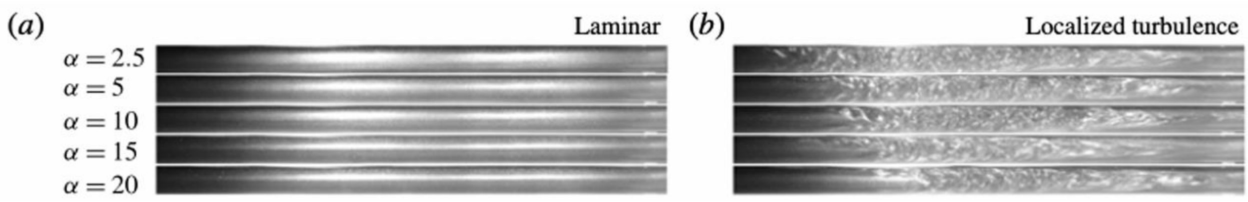

Figure 16: Visualization samples of laminar flow observed in absence of external perturbations (a). When perturbed upstream, turbulence could be excited locally (b). From top to bottom the values of Re are: 3100, 2800, 2500,2500,2500. Flow from left to right [1]

survival probability is defined as the ratio of number of survival cases and total number of runs (for each Re 150 runs were carried out). In steady pipe flow, the probability of surviving for a time t is only a function of Reynolds number: $P(Re,t) = \exp\left[-(t-t_0)/\tau(Re)\right]$ with τ is characteristic lifetime of a puff, t is current timing of the experiment and t_0 is the time for the initial formation of a puff (t_0 is measured to be around $100D/U$). For a steady flow rate, survival probabilities are fully in agreement with Hof et al. 2008 experiments (red circles and black solid curve in figure 17a). The survival probability increases with Re, following a S-shaped curve. The probability P=1 is only asymptotically approached. The S-shaped curve is followed also at fixed amplitude A=0.4 and variable pulsation frequency. For low Womersley numbers the S curves are shifted to the right, resulting in a higher Re to observe puffs of appreciable lifetimes. For large Womersley numbers, survival probabilities are close to the steady pipe flow case and are unaffected by flow pulsation. The measurements at lower Womersley numbers had to be carried out in the set-ups with longer pipes, to guarantee a full oscillation cycle to puffs. Data show that transition thresholds keep increasing with decreasing Womersley numbers, even though there is a slow down for $\alpha < 2.5$ (figure 17b).

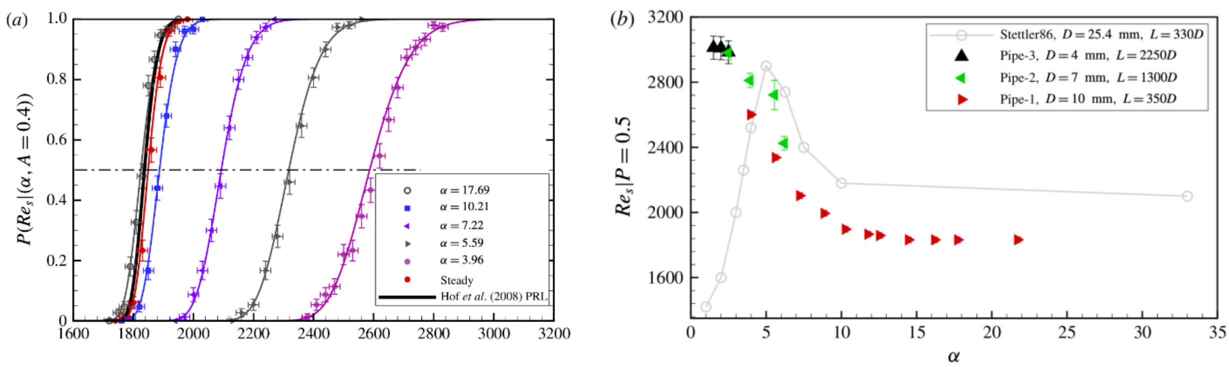

Figure 17: (a) Survival probability of individual puffs, as a function of Re, fixed A=0.4; (b) Reynolds number in function of Wo, for P=0.5 [1]

The influence of the pulsation amplitude on transition was also tested: the experiments were conducted with fixed pulsation frequency and variable A. the S-shaped curves appear shifted to higher Re and the transition delay increases with pulsation amplitude (figure 18a). For all the four frequencies tested, the transition threshold increases monotonically with pulsation amplitude (figure 18b). The transition delay is more evident for low frequencies (low α), whereas for large frequences the increase with amplitude is moderate.

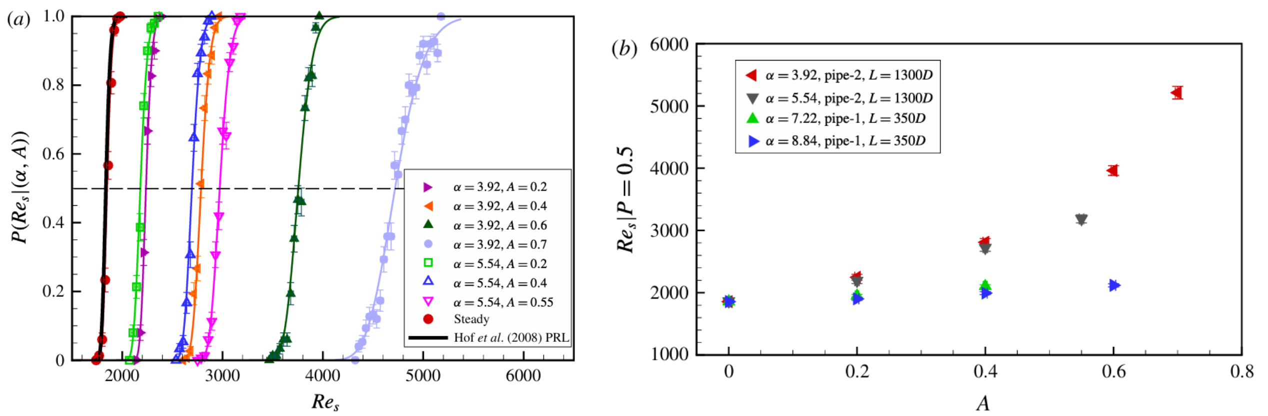

Figure 18: (a) Survival probability of puffs with variable pulsation amplitudes. (b) Reynolds threshold values as a function of A [1]

To sum up the results, puffs are the first turbulent structures that are generated in the subcritical regime of pulsatile pipe flow, and their lifetime provides an accurate measure of the transition threshold. The experiments conducted by Xu et al. lead to the idea that the transition to turbulence in pulsating pipe flow can be divided into three regimes:
(i) For $\alpha > 12$ (large frequency limit) the transition threshold is unaffected by flow pulsation: rate changes are too fast for turbulence to react.
(ii) For $\alpha < 2.5$ the changes of Re are sufficiently slow for the generation of turbulent structures and their lifetime can be predicted by quasi-steady assumptions. During the faster part of the cycle, Re drops and turbulence reduces to puffs: it is a critical condition for the survival of turbulence.
(iii) In the intermediate regime ($2.5 < \alpha < 12$), the transition threshold adjusts smoothly between the two limits.

3.6 Nonlinear hydrodynamic instability experiments

In this section further experiments conducted by Xu et al. [14] are reported. A nonlinear instability mechanism for pulsating pipe flow that gives rise to bursts of turbulence at low flow rates is investigated. This scenario, characterized by shear stress fluctuations and flow reversal at each pulsation cycle, can affect blood vessels and thus be the responsible for a variety of cardiovascular diseases. The inner lining of blood vessels, the endothelium, is particularly sensitive to shear stresses.

The experiments were carried out in a rigid straight pipe with a diameter D of 7mm and a total length L of 12 m. The fluid was pulled through a piston, with a resulting set-up similar (figure 19) to the previous experiments. The piston was sinusoidally modulated.

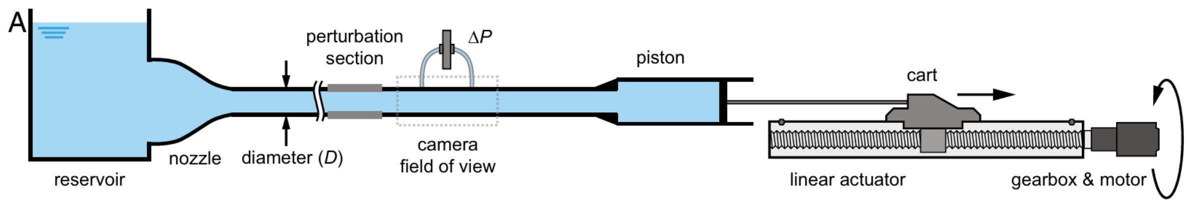

Figure 19: Sketch of the pulsatile flow set-up [14]

3.6.1 Helical instability

The first part of the experiments concerned puff turbulence, giving results in accordance with chapter 3.5: at sufficiently large Re all puffs would survive, with the puff transition depending on the pulsation amplitude (figure 20).

When the pulsation amplitude surpasses 0.7, the puff trend stops, and the transition threshold moves to lower Re (measured on the mean flow speed). Instead of puffs, a regular, helical vortex pattern appears. This structure, unlike puffs, does not depend on the injection of a jet, but develops at a fixed pipe location during each cycle in the deceleration phase, and then decays during acceleration. With a further increase in the pulsation amplitude, the threshold moves to lower Re (figure 20). The instability branch can be continued also for lower amplitudes (A<0.7): puffs are not trigged, but instead the Reynolds number is increased up to the point where the helical instability appears naturally.

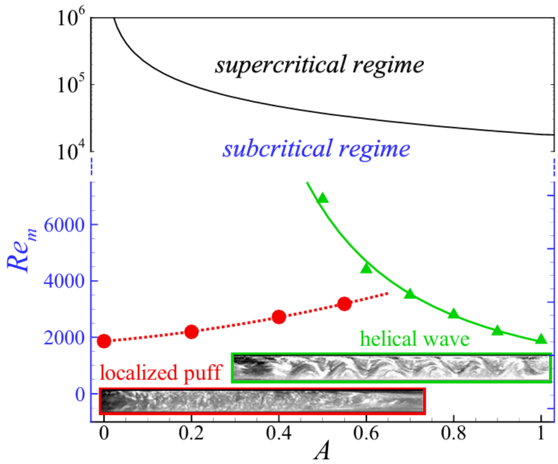

Figure 20: Threshold for the onset of puffs is the red dotted line. That for the onset of the helical wave instability is given by the green one. Fixed Wo=5.6. The black curve shows the linear instability threshold which sets in at much higher Re than discussed [14]

An inspection of the pipe showed that the pipe segment upstream the helical wave instability was slightly bent. By realigning the pipe, the instability switched to larger Re, while increasing the misalignment moved the threshold at lower Reynolds numbers.
A comparison of puffs and helical instability is conducted at the same parameter values (Re, Wo, A) = (2200, 5.6, 0.85) and during the deceleration phase. In one case the pipe was aligned, and a puff was generated by an upstream injection perturbation; in the other case no puff was triggered, and the flow was perturbed by the upstream bent segment pipe. What happened is that the puff spreads in the downstream direction, while the upstream interface remains in the same location, whereas the helical instability spreads both down- and upstream (figure 21). This means that the helical instability is of absolute nature during a cycle phase, while a puff remains convective. The types of disturbance that trigger the helical instability are thus different from those triggering puffs.

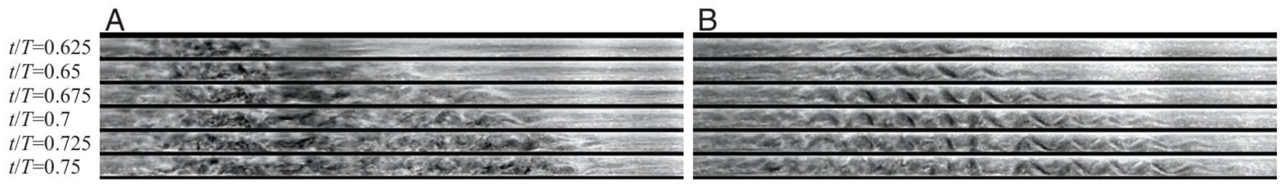

Figure 21: Visualization of transition to turbulence in pulsating pipe flow. (a) Evolution of a puff. (b) Evolution of helical instability [14]

The considered misalignment is only a fraction of the pipe diameter: in the cardiovascular system all blood vessels have deviations from the ideal straight pipe case of that order or larger. Another experiment was carried out with a shorter pipe segment but more strongly curved: the instability occurs at way lower Reynolds numbers and the threshold decreases with the amplitude. These results lead to think that the helical instability is a result of a perturbation of finite amplitude, like the instability to turbulence in steady flow. For the transition in steady pipe flow the threshold is double: Re and amplitude of the perturbation must be large enough. For helical instability it is triple: Re, amplitude of the perturbation and of the pulsation must be sufficiently large.

3.6.2 Blood flow

For these experiments, blood is used as the working fluid: it has non-Newtonian properties and is a dense suspension of blood cells (red blood cells are 40% of the volume fraction). The set-up is scaled down, consisting of a pipe diameter of 4 mm. To trigger turbulence, a curved section was introduced 185D from the pipe inlet. Blood is opaque, which doesn't allow to observe directly the flow structure: for this reason the differential pressure downstream the curved section is monitored. Like Newtonian flows, blood as well becomes unstable during the deceleration phase, with a considerable drag increase at 20D downstream the segment. During the acceleration the flow stabilizes again and returns to laminar conditions. The transition to turbulence for blood flow (orange symbols in figure 22) occurs at lower Reynolds number than for water flows. For pulsation levels typical of the aorta (pulsation amplitude around 0.94), the Re threshold is around 800, way lower than the assumed 2000.

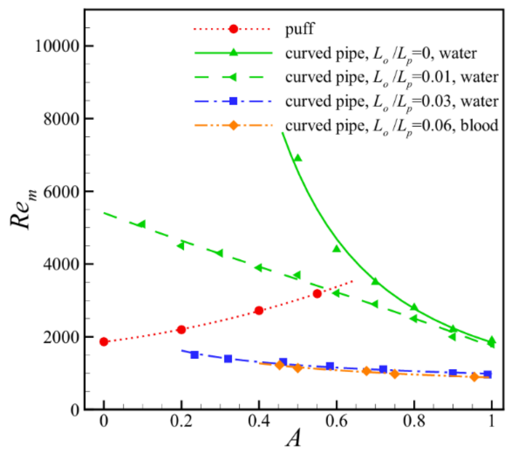

Figure 22: Onset of instability as a function of pulsation amplitude for water and blood. Red circles, Wo=5.6; green triangles, Wo=5.6; blue squares Wo=5.9; orange Wo=4 [14]

3.6.3 Lumen constriction

The cross sections of blood vessels are far away from the idealized circular case: protrusion may arise during wound healing or stenosis formation. It is thus important to study if helical instability can occur in such conditions. The curved pipe segment is replaced by a straight section with a local constriction in the form of a spherical cap (up to D/4 in height). Helical pattern was found in this experiment during the deceleration phase (for Wo=5, A=0.85 and increasing Re). The helical wave was first observed at 40D downstream the spherical cap, and then spreads going from 35D to 55D. The robustness of the helical instability was tested by changing the waveform of the pulsating flow: the sinusoidal profile was replaced by the typical waveform in the aorta. The helical instability was observed again during deceleration and the flow relaminarized again as the flow accelerates.

3.7 Further aspects

In this section, some interesting aspects characterising pulsating pipe flow in the transition to turbulence are examined.

3.7.1 Recirculating fluid

Recirculating flow is a phenomenon that can occur in pulsatile conditions: it is characterized by a region of separation featuring retrograde flow, increased mixing and trapped fluid parcels. A Lagrangian approach to the pulsatile flow behaviour is here reported, with specifical reference to the Jeronimo and Rival [19] work on the lifespan of recirculating suspensions. Experiments are conducted for pure liquid and suspensions with volume fractions of Φ=5%, 10% and 20%. Lagrangian tracking and pathline extension techniques are used to quantify the depletion of the recirculating region, by analysing the trajectories of individual fluid parcels. Pulsatile flows with a varying concentration of hydrogel beads are compared at mean Reynold numbers of 4800, 9600 and 14400, while Strouhal numbers of 0.04, 0.08 and 0.15 and amplitude ratios are systematically varied. A so-called 'depletion efficiency' is calculated for each test case.

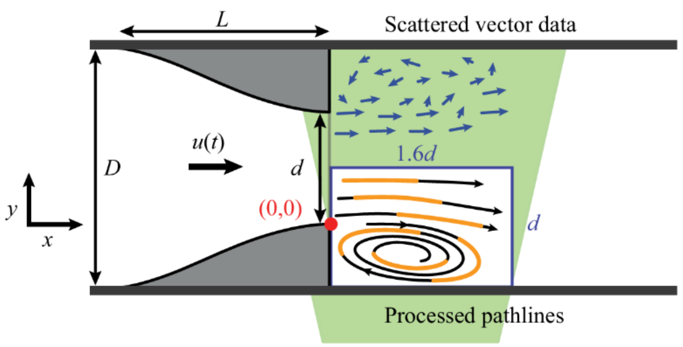

Figure 23: Cross sectional slice, showing the stenosis model [19]

In Jeronimo and Rival study, an idealized stenosis geometry is used to generate a large recirculating region within which the depletion efficiency of pulsatile flow is investigated. What happens for a pulsatile flow is that a vortex ring is generated, then grows, propagates and sheds, thus creating a recirculating zone. The depletion efficiency was evaluated with a set-up (figure 23) including the flow loop and idealized stenosis model (to ensure that turbulent flow conditions are fully developed, the onset of the pipe's constriction is located 60D downstream the nearest corner). The working fluid was pumped from the reservoir with a programmable circumferential piston pump, controlled using LabView. Two-dimensional particle tracking velocimetry (2D PTV) was performed in a 1m long acrylic pipe with D=7.6cm housing the constriction, consisting in a 50% reduction of the diameter (reduction of 75% of the area). A high-speed complementary metal oxide semiconductor camera recorded the flow exiting the throat of the stenosis, with a frame rate up to 2000 Hz. Lagrangian particle tracking of the liquid phase was performed in the downstream region by seeding the working fluid with neutrally buoyant 55 μm polyamide tracer particles (LaVision 1108947). These particles are assumed to reliably follow the motion of the liquid.

The results of this study show a substantial increase in depletion efficiency when pulsatility is introduced (figure 24), at all Reynolds number investigated. The primary depletion mechanism for pulsating flows is a periodic vortex, generated during the initial acceleration of each pulse. These vortex structures entrained and displaced large volumes of fluid and grow in strength with increasing amplitude. Strouhal number has no influence on the amount of the vorticity gained by fluid parcels, but high Strouhal number flow increases the depletion efficiency by a more frequent generation of vortices. This trend applies for both pure-liquid and suspension flows.

To sum up, for what concerns the prevention of accumulation of trapped fluid within a recirculating region, the pulsatile flow is more advantageous than the steady flow.

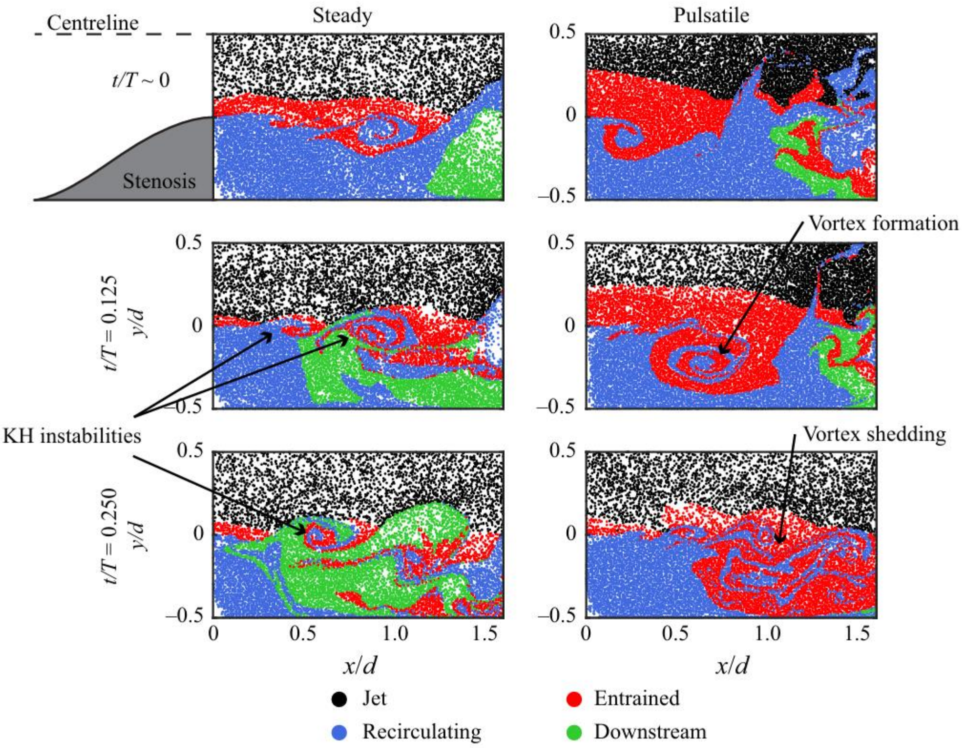

Figure 24: Fluid parcels in the measurement domain are categorized according to their source and trajectory. Vortex formation and shedding is evident for pulsatile flow (on the right) and absent for steady flow (on the left). Both flows are compared at Re=4800, over the same length of time [19]

3.7.2 Transport phenomena

The second aspect concerning turbulent pulsatile flows that is here examined is the one about the transportation mechanism of single solid particles in pulsating pipe flow. The work by Fujimoto et al. [20] investigates this topic, with the aim of understanding how the pulsating nature of the flows influences the motion, distribution and overall phenomena of solid particles. Their study employs both experimental and theoretical approaches to achieve a comprehensive understanding of these topics. In particular, the experiments were carried out with a vertical lifting pipe made of transparent plastic, of a total length of 2870mm, inner diameter varying from 18 to 22 mm. The working fluid was water at room temperature, and it was supplied at the bottom of the lifting pipe: as a result, it flows upwards, discharging at the top, and then returning at the reservoir. Pulsating flow is generated with an electromagnetic valve, that dictates how water is supplied by being controlled with a digital timer. The solid particles used are spherical alumina particles with diameter between 3 and 5 mm. The data is collected through two digital cameras that record particles motion. The experimental data and the numerical simulations resulted into three main aspects:

(i) the particle is lifted upward along the pipe wall in steady upward flows because of the vertical velocity profile of the liquid in radial direction. In pulsating upward flows, the particle has an up-and-down motion. Because of the occurrence of reverse flow near the pipe wall, the particle was located near the pipe wall and then near the centre axis;

(ii) the numerical simulations revealed that the liquid velocity profile is almost flat near the centre axis in pulsating pipe flow with small C_{ratio} (ratio of constant volume flow rate to the total volume flow rate, values between 0 and 1; if C_{ratio}=1 the flow is steady). With increasing C_{ratio} the flow approaches steady-state distribution;

(iii) the critical minimum flux for transporting single particles depends on the pulsating pattern.

Figure 25 shows the typical motion of an alumina particle in a steady flow and in a pulsating upward flow.

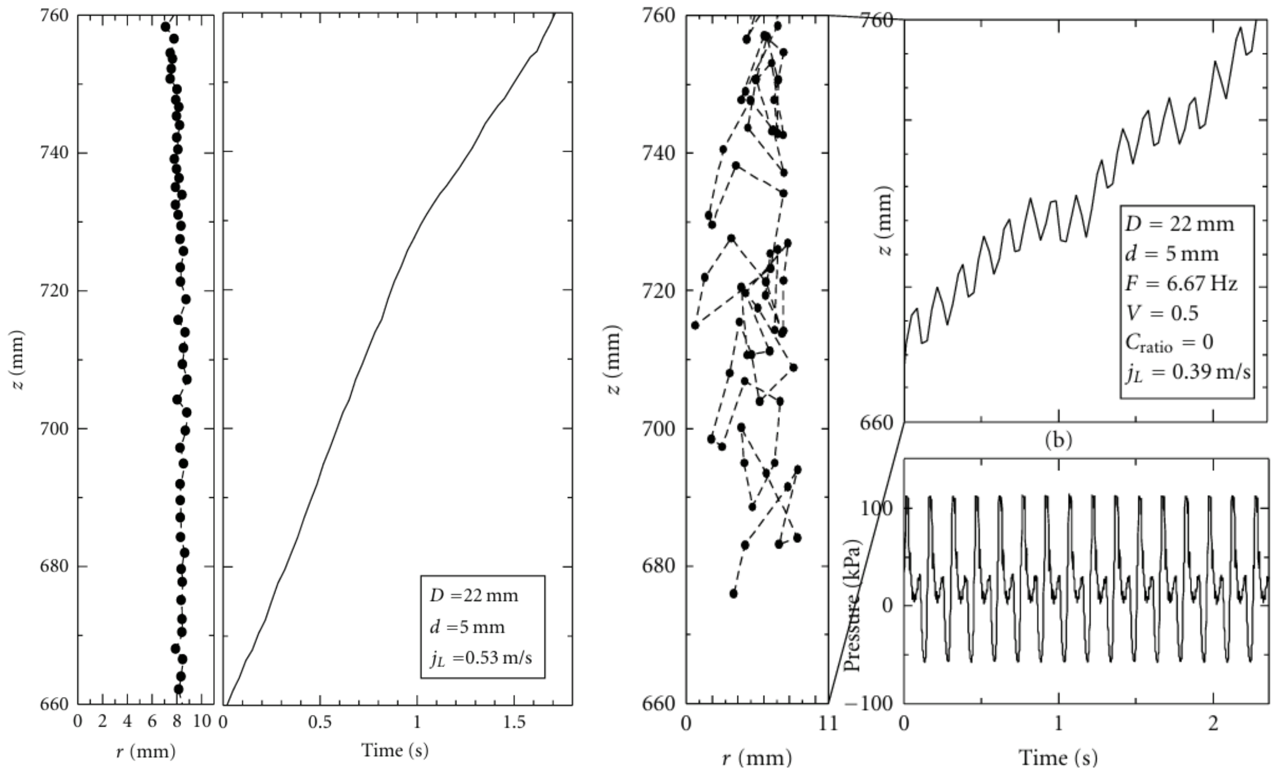

Figure 25: Typical motion of an alumina particle in a steady flow and in a pulsating upward flow [20]

3.7.3 Time-delayed characteristics

A study was conducted by Xu et al. [17] to investigate time-delayed characteristics of turbulence in pulsatile pipe flow, using direct numerical simulations. The topic of interest is the paradoxical phenomenon where the amplitude of the oscillating wall shear stress in turbulent flow is smaller than in laminar flow under same pulsation conditions. The focus is on the temporal variations of wall shear stresses and flow dynamics to provide insights into the delayed response of turbulence in the buffer layer, that suggests a turbulence-induced drag reduction opposite to that in the steady flow. This delay in response plays a crucial role in reducing the amplitude of the wall shear stress in comparison to laminar stress.

It is shown that the delayed response of turbulence in the buffer layer generates a large magnitude of the radial gradient of the Reynolds shear stress near the wall, counteracting the effect of the oscillating pressure gradient and thus reducing the amplitude of the wall shear stress. This delayed response consists of two processes: the delay in the development of near-wall streaks and the subsequent energy redistribution from the streamwise velocity fluctuation to the other two co-existing components. An examination of the energy spectra reveals that the near-wall streaks are stretched in SW direction during acceleration phase, and then break up into small-scale structures in the deceleration phase, along with an enhanced dissipation transforming the turbulent kinetic energy into heat.

Figure 26 depicts the temporal evolution of instantaneous space-averaged wall shear stress τ_w: the red solid lines represent the laminar values. Four different cases are reported: (a) and (b) low-amplitude cases (A=0.1), (c) and (d) high-amplitude cases (A=0.4). For low-amplitude cases all the curves are evenly dispersed, while for high-amplitude cases local scattering of the curves can be observed. Such a localized scattering of the wall shear stress curves indicates that the delayed response of turbulence in the drag-reducing phase is an intense event, characterized by randomness as well. The higher the pulsation amplitude, the more intense the turbulence response.

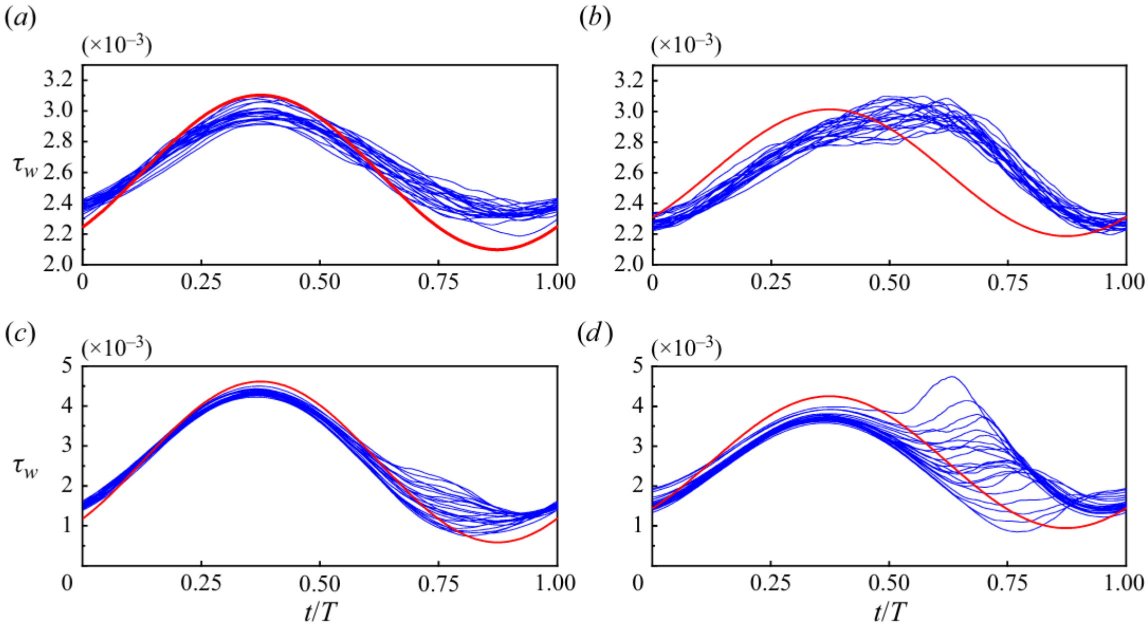

Figure 26: Temporal evolution of instantaneous space-averaged wall shear stress [17]

3.7.4 Effects of waveform

Moron et al. [16] carried out some experiments to study the effects of waveform on the transition to turbulence. The approach to study these effects starts with the definition of the waveform itself, which is done by fixing only tree parameters. First, six control points (black stars in figure 27) are defined, giving an idea of the skeleton of the generic waveform. The position of these points is linked to the three key parameters (t_{ac}, t_{dc} and t_m), that are independent from the mean velocity and don't affect it at all. A cubic spline is then defined so to capture the position of the control points.

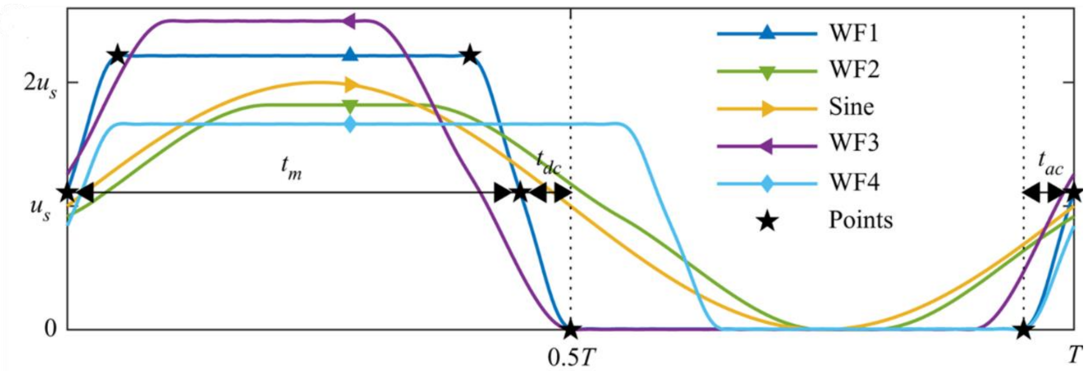

Figure 27: Definition of the generic WF: temporal evolution of the bulk velocity over one pulsation period. The black stars denote the six control points; the solid lines represent the 30 Fourier mode approximation of the spline that passes through these points [16]

Four different waveforms were defined in the experiments. They are all characterised by an acceleration phase, with a slope set by the parameter t_{ac} (note that the total duration of the acceleration is $2t_{ac}$ long). The bulk velocity remains in a high-velocity phase for the time span $t_m - t_{ac} - t_{dc}$. Then the pulsation enters a deceleration phase, where the slope is again linked to the key parameter t_{dc} (total duration of acceleration is $2t_{dc}$). The bulk velocity now enters a low-velocity phase for the rest of the period T. The parameter t_m also sets the maximum Re of the flow as $Re_{max} = Re\frac{T}{t_m}$. For $t_m = T/2$ the waveform is symmetric and the high- and low- velocity phases have the same duration.

From the experiments of Moron et al. it was found that the helical perturbations, reported in section 3.6, are linked to the instantaneous linear instability of the laminar velocity profile in pulsatile pipe flow. This instability is due to the presence of inflection points in the laminar profile and their characteristics. Moron er al. found that for the instability to grow, two requirements must be fulfilled. The first one is the existence of inflection points that satisfy the Fjørtoft criterion and instantaneously make the laminar profile unstable for a sufficiently long fraction of the period. This requirement is satisfied for Wo>3 and A>0.5. The second is that the laminar profile evolves slower than the perturbations, which is satisfied for Wo<17. In the range of Re investigated, these two requirements mean that the laminar profile is highly susceptible to the growth of the perturbations, during the fraction when inflection points occur. This happens typically during the deceleration phase, when the helical perturbations present an outstanding energy growth.

The waveform of the pulsation can change the characteristics of such inflections point, in particular their lifetime and radial span. For waveforms with longer low-velocity phases (smaller t_m) , the inflection points have a longer lifetime, thus resulting in more time for the perturbations to grow. In addition, the more abrupt the acceleration and the deceleration are (smaller t_{ac} and t_{dc}), the higher the chances for perturbations to grow. This has a result that by simply knowing the waveform and the flow parameters, it is possible to estimate the growth of perturbations for a certain pulsatile pipe flow, with no need of computing the velocity profiles.

The waveform also influences the turbulence survival once the turbulence is triggered. In contrast to what was found for the role on the perturbation growth, flows driven by waveforms with small t_m, t_{ac} and t_{dc}, promote turbulence decay. This suggests that, in the non-linear regime, the waveform has additional effects, e.g. waveforms more susceptible to perturbations growth are more prone to cause relaminarisation once the flow is turbulent.

4. Transition of pulsatile flow under different configurations

In this chapter the transition to turbulence of pulsatile pipe flow is still examined, but for configurations differing from the ideal straight, circular pipe, that was investigated in the previous section. Some of the configurations here presented have already been slightly discussed above, but here are studied with a deeper look. In particular, the influence of the following factors is examined: constricted pipes, curved pipes, compliant walls and roughness. Their discussion is treated with a constant reference to cardiovascular flow and possible medical applications. But first, an introduction on blood flow behaviour in arteries [21] and the influence of turbulence on it are presented.

4.1 Cardiovascular system and turbulence

The cardiovascular system has two primary functions: nutrient and waste transportation throughout the body. The blood is distributed through a network of vessels. The arteries adapt to varying flow and pressure conditions by enlarging or shrinking depending on the hemodynamic demand. Blood, being a complex mixture of cells, proteins, lipoproteins and ions, is very viscous, approximately four times more than water. As already mentioned in section 3.6.2, blood does not exhibit a constant viscosity at all flow rates and is especially non-Newtonian in the microcirculatory system. However, in most arteries, blood behaves in a Newtonian way: the viscosity can be assumed constant (4 centipoise).
Blood flow and pressure are unsteady. The cyclic nature of heart pump creates pulsatile conditions in the vessels: the heart ejects and fills with blood in alternating cycles (systole, when blood is pumped out, and diastole, no blood is ejected). Pressure and flow have specific pulsatile shapes that are different in the parts of the arterial system. The blood pressure is pulsatile in most arteries, without going to zero during diastole. In some arteries, the flow can be zero or even reversed during diastole. The typical Reynolds number range of blood flow in the body varies from 1 in small arterioles to approximately 4000 in the aorta, the largest artery. Reynolds number and Womersley number are good parameters to understand blood flow, even though they do not consider certain features of biological flows: vessel wall elasticity, non-Newtonian viscosity, slurry particles, body forces and temperature.
Several pathologies may arise from an excessive or uncontrolled response to a hemodynamical stimulus. Long-term hypertension produces a generalized medial thickening of blood vessels. Thick and stiff arteries restrict blood flow and do not respond to the normal physiologic fluctuations in blood flow. Stenoses may arise and occlusion may happen, especially in small diameter vascular grafts. High shear conditions may overstimulate platelet thrombosis, causing a total occlusion. If vascular grafts are too large in diameter, wall shear stress is abnormally low, and an intimal thickening may be stimulated

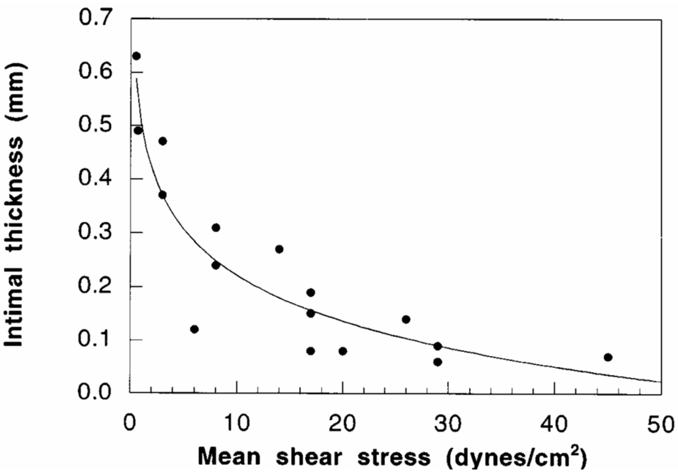

Figure 28: Atherosclerotic intimal thickening vs wall shear stress in human carotid arteries [21]

(figure 28). Atherosclerosis forms over decades in localized sites of some arteries, where the mean wall shear stress is very low, oscillating between positive and negative directions.

Turbulent pulsatile flow can lead to one of the most catastrophic diseases that can affect the Aorta: aortic dissection, which is the combination of a tear in the inner layer of the aortic wall communicating with a false channel (dissection) cleaved through the media layer of the aortic wall. Tear and dissection appear in the aorta when the stresses on the wall rise beyond the elastic limit. With numerical simulations it is possible to predict what conditions determine the level of dissection that will occur. Results from the study of Khanafer and Berguer [22] on aortic wall dissection are here reported. They investigated a FSI (fluid structure interaction) model within a three-layered aortic wall under turbulent pulsatile flow condition as related to aortic dissection.

When the bulk flow starts to decelerate, the velocity in centreline of the lumen decreases as well until the flow is reversed. It is accepted that the intimal tear occurs when the stress on the wall during the cardiac cycle exceeds the mechanical failure strength of the wall. The effect of flow dynamics on the aortic wall stress distribution is investigated in terms of Von Mises stress.

$$\sigma_{VM} = \sqrt{\frac{(\sigma_1-\sigma_2)^2+(\sigma_1-\sigma_3)^2+(\sigma_2-\sigma_3)^2}{2}}$$

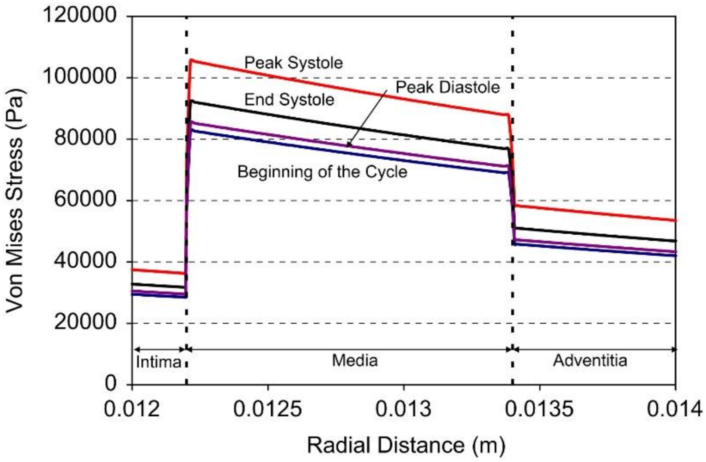

Figure 29: Variation of the Von Mises wall stress across the wall of a descending aorta at various periods of the cycle [22]

As shown in figure 29, the stress distributions are discontinuous at the interface between layers because of the difference in the mechanical properties: the jump in the stress value between intima and media layers is higher than media and adventitia (the external one) layers. The stresses are highest in the media layer and lowest in the intima layer.

Turbulence kinetic energy and frequency are maximum at peak flow condition and are confined to a narrow region along the wall of the lumen. Cyclic turbulent stresses in flowing blood may cause damage to red blood and endothelial cells. The smallest turbulent eddies, which are a function of the kinematic viscosity of blood and turbulent dissipation rate, can mechanically damage the blood cells and the components of the arterial wall.

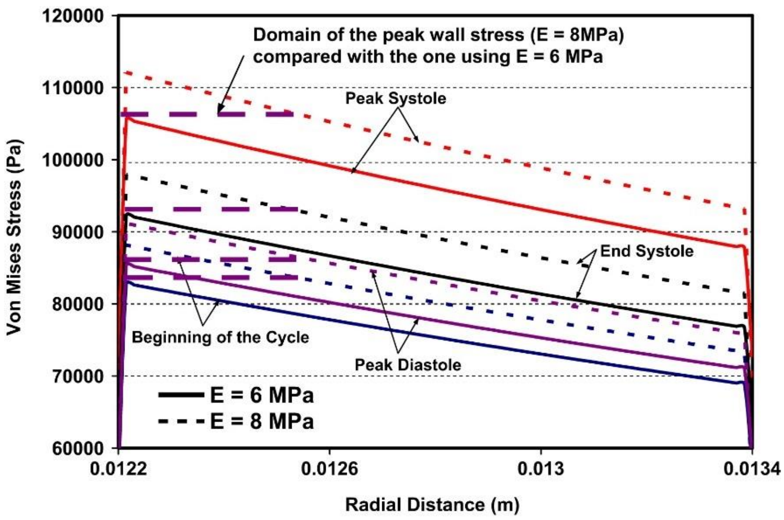

Figure 30: Effect of varying the elasticity of the media layer on the Von Mises wall stress distribution [22]

The numerical approach also showed that the difference in the elastic properties of different layers of the aorta wall may contribute to the occurrence of dissection in the media layer, where the wall stresses are larger. Figure 30 shows that as the elasticity of the media layer increases, wall stress increases. Peak Von Mises stress is found to increase by 6% at peak flow condition, from E=6MPa to E=8MPa.

4.2 Constricted pipe

Hemodynamics is a very important research topic for its implications in cardiovascular diseases. Atherosclerosis, in particular, is a disease that is characterized by the formation of plaques that narrow the arterial lumen, thus resulting in the hardening of the arteries. Localized atherosclerotic constrictions in arteries, known as arterial stenoses, are found predominantly in the internal carotid artery which supplies blood to the brain, the coronary artery which supplies blood to cardiac muscles, and the femoral artery which supplies blood to the lower limbs [25]. Blockage of more than 70% (by area) of the artery is considered clinically significant as it presents significant health risks for the patient: the narrowing of the coronary arteries can stop the profusion of blood to the lower parts of the myocardium and possibly lead to myocardial ischemia, myocardial infarction and sudden cardiac death [28]. Complete closure of the artery can occur if a blood clot becomes lodged in the stenosis, and this can lead to a stroke or a heart attack. Moderate stenoses should as well be monitored as they can have long-term health consequences. First, the presence of a constriction results in head losses which can reduce the blood supply through the artery and also impose additional load on the heart. It is found that these pressure losses are significant when the internal diameter is reduced beyond about 50%. Second, the fluctuations in the blood flow downstream of the stenosis can damage and weaken the internal wall (intima) of the artery. The variability in wall shear can prevent endothelial cells of the intima from aligning in the direction of the flow, thereby making the intima more permeable to the entry of harmful blood constituents. Fluid dynamics of post-stenotic flow also plays a key role in the diagnosis of arterial disease: periodic shedding of vortices downstream of the constriction causes arterial murmurs. Through the analysis of the sound spectra of the arterial murmurs it is thus possible to predict the severity of the stenotic occlusion.

Direct numerical simulation and large-eddy simulation have been used to study pulsatile flow in a channel with a one-sided semicircular constriction over a range of Reynolds number from 750 to 2000 [25]. Please note that channels have a similar behaviour to pipes. When subjected to pulsatile flow, the studied geometry reproducing stenosis produces complex turbulent flow, rich in vortical structures and large recirculating regions. The aim is to understand the dynamics of flows downstream of severe arterial constrictions. With a fixed Strouhal number of 0.024, along with the chosen Reynolds number, the blood flow in the larger arteries of the human cardiovascular system is simulated. Examination of the vortex dynamics indicates that the dynamics of the flow downstream is dominated by two shear layers, one of which separates from the lip of the constriction and the other from the lower wall. Mean flow and pressure distribution computed over a number of cycles indicate a relatively large mean recirculation region on the side of the constriction, and the size of it reduces with increasing Re. There is a significant drop in the pressure across the constriction because of the increased mixing induced by the shear layers downstream of the constriction. The mean recirculating zones are associated with low values of skin friction. The mixing of these regions increases with increasing Re [26]. For what concerns these regions, it is interesting to measure particle residence time (PRT) [31].

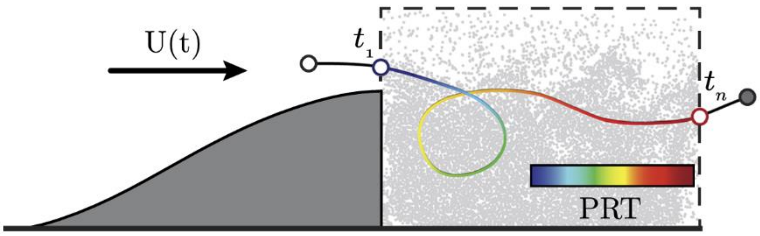

Figure 31: PRT is visually described by the particle pathline that enters a measurement domain (dashed box) at t1 and exits at tn. The pathline's colour represents the instantaneous growth of the particle's PRT as it remains in the domain [31]

PRT is a path-dependent quantity that highlights regions of recirculation and stagnation by tagging fluid parcels in a Lagrangian framework. It is potentially an invaluable tool for a wide range of fluid scales, including biomedical, environmental and industrial flows. For the medical field, PRT is of particular interest to study thrombosis growth and atherosclerosis. PRT is defined as the length of time a fluid parcel remains within a region of interest, normalized by the periodic motion of the flow, such that PRT = $(t_n - t_1)/T$ (T period of the unsteady waveform), in reference to figure 31.

Figure 32 (multimedia view) shows the movement of fluid exiting the stenosing, at St=0.15 and λ=0.50, over a single pulse. The colour labels make a clear distinction between particles that form a jet exiting the stenosis throat and those that have slowed or changed direction in the recirculating region. With each pulse, a large influx of fluid circulates back into the domain from downstream, displacing low velocity particles. As figure 32 shows, during the initial acceleration phase of each pulse and at each mean Reynolds number, a large vortical structure forms, sweeping particles from the jet deep into the recirculating region. The creation of a vortex ring with each pulse is a fundamental feature of pulsatile flow through a stenosis (discussed also in 3.7.1). As the flow decelerates, the vortical structure rolls up and an influx of downstream fluid displaces high-PRT blue particles. As the mean Reynolds number increases, the fluid recirculating from downstream, does not penetrate as far toward the stenosis wall. As a result, there is less fluid flushed from the

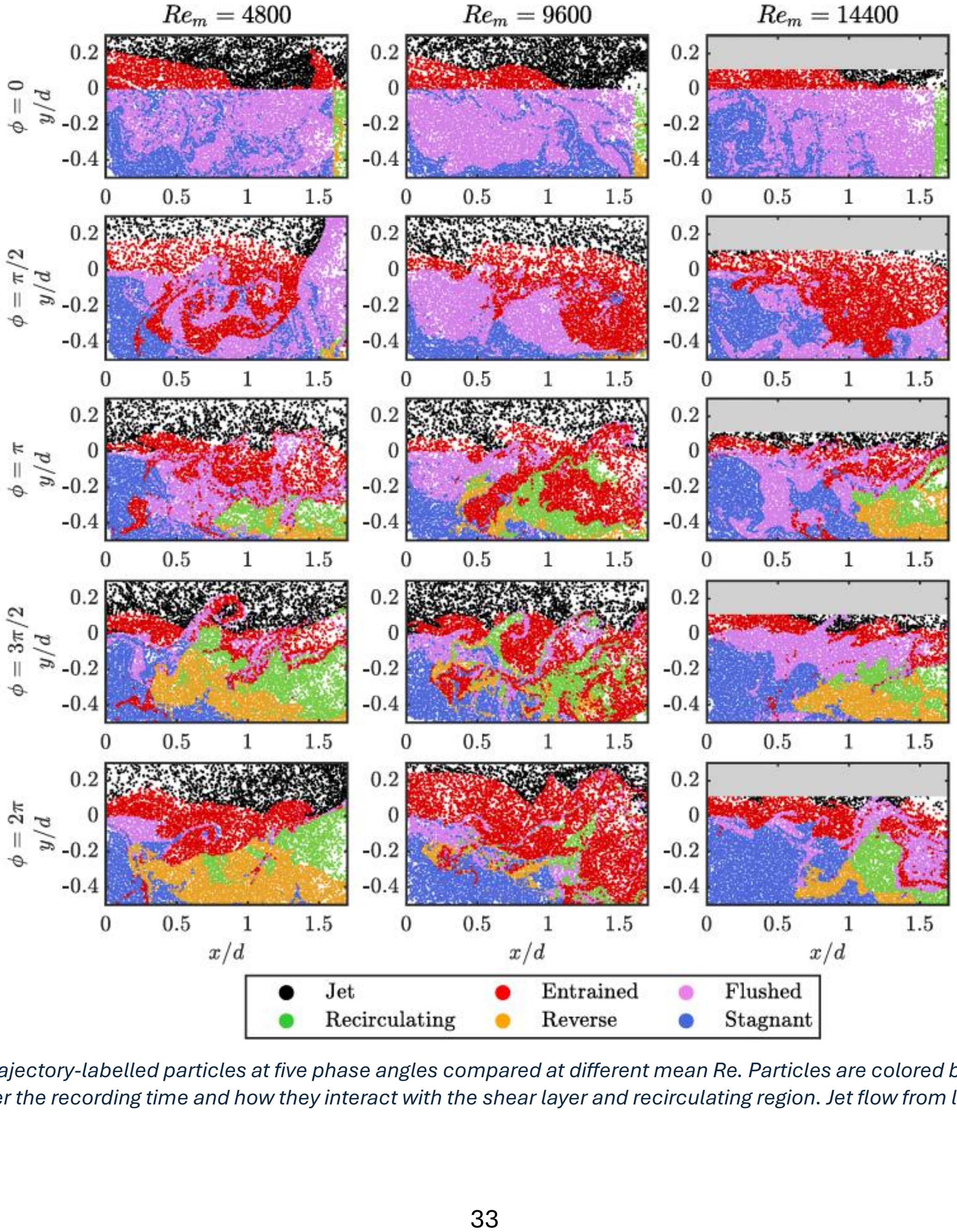

Figure 32: Trajectory-labelled particles at five phase angles compared at different mean Re. Particles are colored based on their trajectory over the recording time and how they interact with the shear layer and recirculating region. Jet flow from left to right [31]

domain with each pulse at high Re_m and there are more stagnant high PRT particles at the end of the cycle. To calculate the PRT, particle track lengths within the measurement domain are used. Figure 33 compares the instantaneous PRT, normalized by period, of pulsatile flow at each of the three mean Reynolds numbers, for the same values of figure 32 (the particles are the same). It is possible to differentiate between particles that remain within the domain (blue - high PRT), which are confined to the jet (black - low PRT) or are mixed into the recirculating region (red - dependent on flow conditions). The average PRT of particles remaining in the domain increases substantially with the Reynolds number. What also is observed is: a decrease in PRT with the increase of mean jet velocity; an increase in PRT with Strouhal number, at every combination of Re_m and λ; increased PRT correlated to augmented mixing from the jet into the recirculating zone and to increase amplitude ratio. These results suggest that elevated heart rates and strong velocity gradients, promote recirculation and stenotic growth.

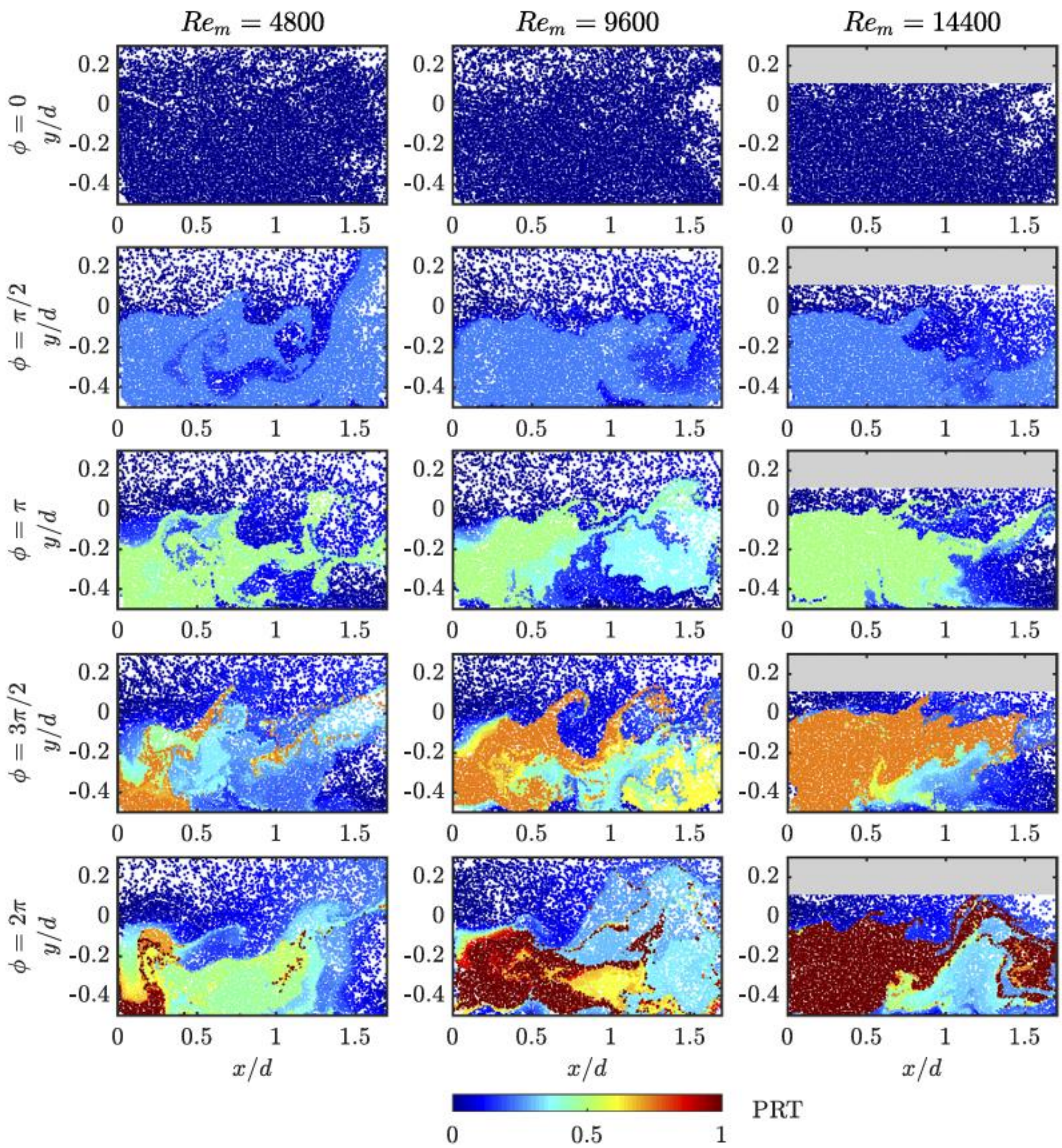

Figure 33: The same particles from figure 32 are labelled by their instantaneous PRT. The PRT grows as a particle remains in the measurement domain [31]

To sum up, in a pulsatile flow, the alternating phases of acceleration and deceleration promote particle flush out and stagnation, respectively, and result in shorter mean PRT. However, isolating the particles that have passed through the stenosis show more mixing across the shear layer and longer PRT in the unsteady case.

Coming back to the general discussion about downstream flow of the constriction, in order to characterize its complex dynamics, flow variables must be decomposed into a phase average and a fluctuation. The phase average is directly associated with the flow pulsation, including the time-mean and low-frequency portion of the variation. The fluctuation contains only the high-frequency portion. As the Reynolds increases, vortex structures become more energetic, leading to an increase in the turbulent kinetic energy. Another consequence is the increasing dissipation, that tends to diminish the turbulent kinetic energy faster for higher Reynolds number cases. By examining wall pressure fluctuations, it appears that the highest intensity occurs 3-4D downstream. In this region also the fluctuation of wall shear stress is the highest, thus having implications for the localization of arterial pathologies. The frequency spectra corresponding to the pressure fluctuations have reported that in the region occupied by the separated upper shear layer, the pressure spectra also exhibit a clear peak corresponding to the periodic vortex formation. Further downstream, the pressure spectrum indicates a break in slope at roughly the frequency corresponding to the characteristic frequency of the lower shear layer. Wall pressure fluctuation spectra show that there is a sharp break in the slope at a frequency corresponding to the shear-layer frequency. This has implications for the analysis of arterial murmurs. If the hypothesis that arterial murmurs are primarily caused by wall pressure fluctuations, then, according to these results, the signature of the shear-layer frequency should clearly be present in the frequency spectrum of the arterial murmurs.

For what concerns transition to turbulence, the frequency spectra corresponding to the streamwise velocity indicate that even at the highest Reynolds number of 2000, the flow up to the region where the separated shear layers attach to the channel walls is at most transitional in nature. Downstream of this region, as the shear layer undergoes transition, the vortex structures associated with the shear layers experience complex interactions among themselves and the wall. This finally results in a turbulent flow which exhibits a well-defined inertial subrange, at least for the higher Reynolds numbers. At Reynolds number lower than 1000, no inertial subrange is observed, suggesting that in this range, there is never a full transition to turbulence. The influence of constriction on the transition to turbulence in pulsatile pipe flow is large. Constrictions induce high shear stress, vortex formation, flow separation, and instabilities, which interact with the oscillatory nature of pulsatile flow to promote early transition to turbulence. Understanding these mechanisms is crucial for applications in engineering and biomedical fields, where managing flow stability can help the design of systems and medical interventions.

An experimental study of transitional pulsatile flow with stenosis was carried out using time-resolved PIV and a MEMS wall-shear stress sensor, at mean Reynolds number of 1750 and Wo=6.15 by Ding et al. [29]. The stenosis was modelled by a sinusoidal function, representative of pathology specimens. The pulsatile velocity profile used is close to a patient-specific velocity profile, where the maximum velocity is found at t/T=0.06 (figure 34). The most of basic elements, if not all, of blood flow that are associated with the vascular disease can be found in such a simple flow configuration, which include the transition to turbulence, relaminarization, unsteady flow separation, shear layers, flow reattachment, recirculation regions and wall-shear stress fluctuations. At the start of the pulsatile cycle, a strong shear layer develops from the tip of the stenosis, increasing the flow separation region. The flow at the throat of the stenosis is always laminar due to acceleration, which quickly becomes turbulent through a shear-layer instability under strong adverse pressure gradient. At the same time, a recirculation region appears over the wall opposite to the stenosis, moving downstream in sync with the movement of the reattachment point. The shear-layer weakens as the flow decelerates later in the cycle, which is accompanied by an upstream shift of the reattachment point. The behaviour of pulsating flow during the acceleration phase of both 25% and 50% stenosis cases is similar to that of the steady flow. However, the transition to turbulence is more dominant for the 50% stenosis. With an increase in stenosis to 75%, the accelerating flow is directed toward the opposite wall, creating a wall jet. The shear layer from the stenosis bifurcates: one moves with the flow separation region toward the upper wall; the other moves with the wall jet toward the bottom wall. The wall-shear stress always takes the maximum value at the throat of stenosis, although no fluctuations are observed there due to local flow laminarization. Immediate downstream of stenosis, however, the wall-shear stress is temporarily reduced as the stenotic flow is entrained into the flow separation region. Low wall-shear stress fluctuations are found at two post-stenotic locations: one immediately downstream of the stenosis over the top wall (stenosis side) and the other in the recirculation region on the bottom wall (opposite side of the stenosis). The latter can only be found for the 25% and 50% stenosis. No recirculation region on the bottom wall is found for the 75% stenosis.

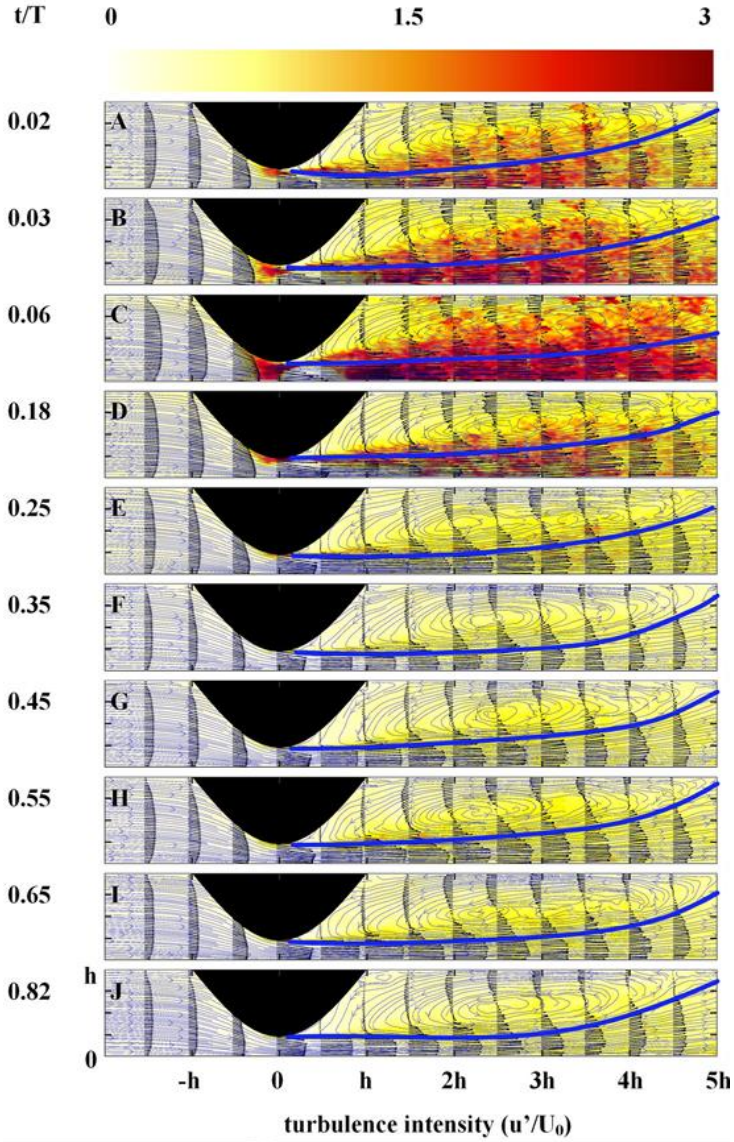

Figure 34: Phase-averaged pulsatile flow at the mean Reynolds number of 1750 with 75% stenosis. Peak Reynolds number is 3200 at t/T=0.06. The contour maps of streamwise intensity is presented here. Blue lines indicate flow separation and recirculating regions [29]

4.3 Curved pipe

Curved pipes influence as well turbulent pulsatile pipe flows, because of their unique geometry and the resulting flow dynamics. When a fluid flows through a curved pipe centrifugal forces have to be taken into account as they cause secondary flows, that are not present in straight pipes. The secondary flows appear as two counter-rotating vortices, thus overlapping the primary axial flow. The interaction between primary and secondary flows is very complex and leads to a variety of effects on the flow.

One of the primary consequences of flow in curved pipes is the development of Dean vortices, named after W.R. Dean (1896-1973). This type of vortices arises because of the centrifugal force on the fluid flowing through the curve, causing fluid particles near the pipe wall to move radially outward and those near the centre to move inward (figure 35). The result is a pair of counter-rotating vortices, causing alterations in the velocity profile. The core is surrounded by a thin Stokes layer on the wall (figure 36) [38]. If the curvature is significant, the axial velocity distribution is entirely altered by the secondary flow, and a considerable increase in resistance is observed. The extent of the above inviscid core increases with further increase in the Womersley number. This secondary flow increases the complexity of the turbulence within the pipe, by interacting with the oscillatory nature of the primary flow. This interaction may lead to an increase in turbulent intensity and energy dissipation, especially during the deceleration phase, thus increasing the likelihood of transition to turbulence. The pulsatile nature of the primary flow can amplify the centrifugal effects: the consequence is a more pronounced secondary flow and greater mixing.

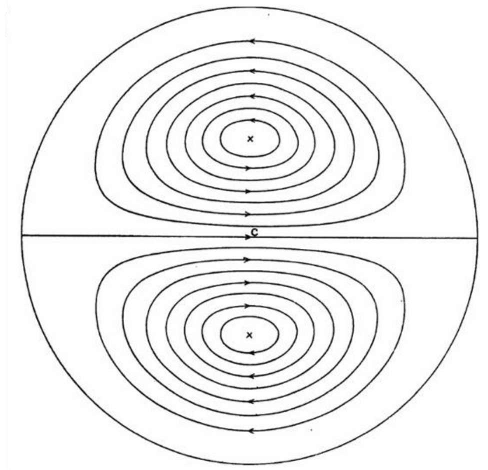

Figure 35: A schematic of the Dean vortices as sectional streamlines [38]

An additional difference from straight pipes is that separation and reattachment points in curved pipes: in this last case, flow separation occurs generally at the outer wall of the bend because of the adverse pressure gradient that the centrifugal forces induce. The flow reattaches further downstream, generating recirculation regions and complex vortical structures. These regions create difficulties in determining overall pressure drop and energy losses. Experimental results show that essentially fully developed conditions for oscillatory flow in curved pipes are achieved within about 90° through the curve, while for large Womersley numbers, regions with strong secondary streaming are observed at the inlet of the curved section.

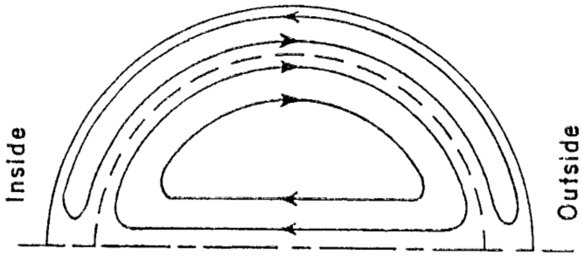

Figure 36: Schematic diagram of the streamlines in the plane of the cross section [38]

The influence of curved pipes on the transition to turbulence of pulsatile pipe flow is still an unexplored area [33]. It was shown that the flow in a curved pipe can remain laminar for substantial higher values of the Reynolds number, compared to a straight pipe. This is because the curvature has a stabilizer effect on the flow.

Moving to the context of biomedical applications, curvature of arteries, accompanied by pulsatile blood flow, may result in the development of disturbed flow patterns, typically involved in the development of atherosclerosis. This disease forms in regions with low wall shear stresses, characteristic of the segments downstream of curved and bended arteries. On the other hand, localized zones of high shear stress can also occur, resulting in mechanical damage to endothelial cells of the arteries, leading to other vascular diseases.

Figure 37 [33] shows the contour plots of the velocity fields obtained through reconstruction, with cross section 0.2D, Re=24000, Wo=41, γ=0.4 (defines curvature). Five pulsating flow fields are shown for the corresponding phase angles indicated (1-5) in the centreline signal of the streamwise velocity. Streamwise velocity scaled by the bulk speed is shown as the background contour map, whereas the in-plane components are shown as the vectors. The flow structured were captured during one pulsation cycle and four main patterns are found: during acceleration and deceleration the flow pattern resembles the one of steady flow with two symmetrical vortices observable; at the peak of the acceleration weak secondary motion exists, while at the end of the deceleration phase the vortices overtake the whole cross section, but with the centres located at the centreline of the pipe.

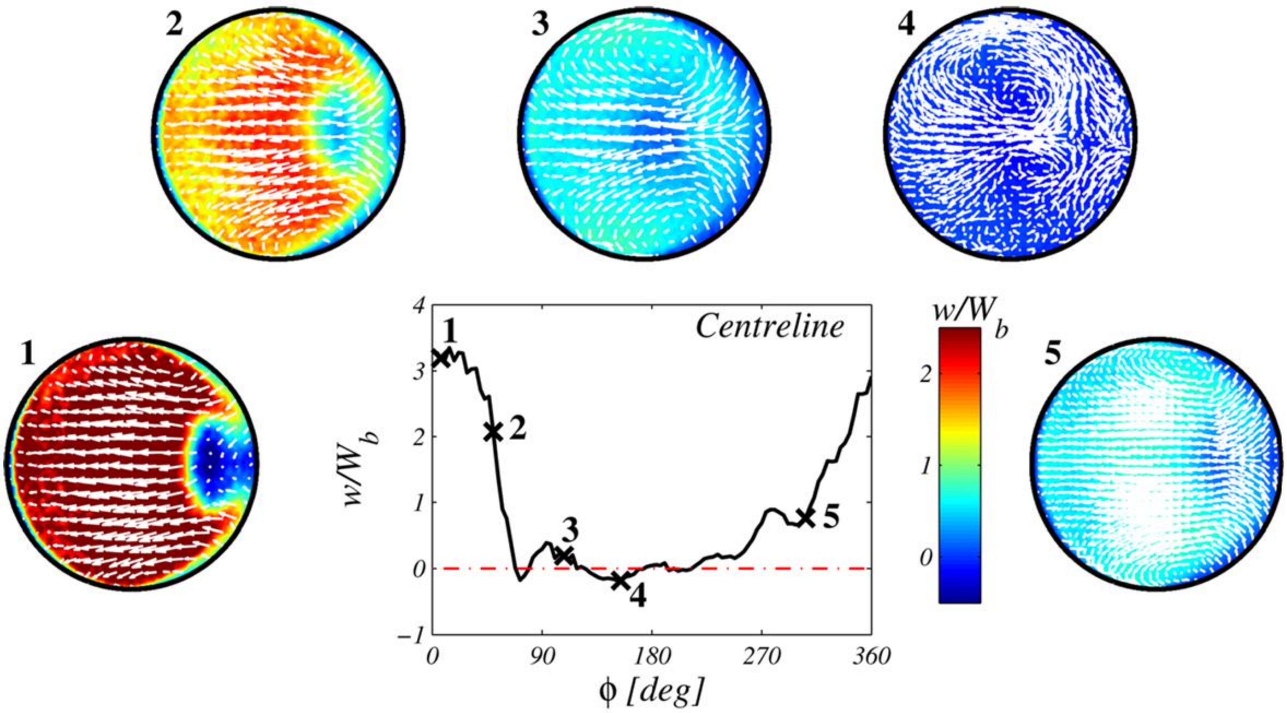

Figure 37: Contour plots of the velocity fields corresponding to five phase angles [33]

4.4 Compliant walls

The nature of flow patterns in rigid and compliant asymmetric constricted pipes for a range of dimensionless parameters typical of human arteries is here investigated. The peak Reynolds number range is Re=300-800 and Womersley number Wo=6-8. The considered pulsation frequency is 1.2-2.4 Hz. In the experiments conducted by Usmani and Muralidhar [24], rigid models are made of glass, whereas the compliant arterial models are made of silicone elastomer, both resembling a diseased vasculature. Asymmetric stenosis experiences localized transition to turbulence with instability occurring in the shear layer. The model is mounted with the axis vertical, which is also the primary flow direction. From PIV imagery it is possible to obtain temporal distribution of stream traces, wall shear stress and the oscillatory shear index (OSI).

For the rigid model (figure 38), a considerable variation over the pulsation cycle is observed. For Re=300, flow remains attached during systolic phase. At peak flow, the instantaneous Reynolds number is high resulting in an adverse pressure gradient over the constriction: the result is a small region of flow separation downstream of the throat. As deceleration starts, the adverse pressure gradient strengthens, streamlines pass smoothly over the throat with an attached vortex in the concavity. The vortex grows as the flow decelerates. Flow reversal carries the vorticity upstream and another starting vortex is formed above the constriction. It is then washed away as soon as the flow starts accelerating again. On the side without the constriction, the flow remains fully attached.

For the rigid tube the wall deformation was smaller than the pixel resolution of the camera, thus resulting in non-deformable wall. For walls less thick deformation can be studied: for 3 mm wall thickness, deformations are small and their variation is almost proportional to the wall loading itself; for 1.5 mm wall thickness, large deformations can be observed. This is the case of compliant models, characterised by fluid-forces producing time-dependent wall deformation that, in turn, alters the flow itself. For small-amplitude wall displacement, fluid flow and wall movement can be expected to be correlated in time, the correlation diminishing with increasing amplitude. At Re=300, wall displacement amplitude is less than 5% of the pipe diameter, while the peak wall velocity amplitude is 5-10% of that of the main flow. These are small but large enough to bring in noticeable changes in the flow pattern. Figure 39 shows flow in compliant walls characteristics. Differences from the rigid case arise from velocity changes related to the cross-sectional area when the walls move inward and outward the cycle. Wall velocities serve to energize the fluid and weaken vortex strength. Vortices are transported more readily in a compliant model compared to the rigid.

During the systolic phase (phase A), the wall moves outward, resulting in lower velocities, smaller adverse pressure gradient and attached flow. Beyond the peak phase, the wall moves inward, and larger velocities strengthen the adverse pressure gradient beyond the constriction. Flow separates from the wall at phase B, increasing in size during deceleration phases (from C to E). The vortex grows, covering most of the post-stenotic region (E), accompanied by further inward movement of the wall. During flow reversal, vortices are weakened and washed away (F). The vortex at the constriction breaks into two and moves upwards (G). A downward vortex is subsequently generated, that will be washed away.

At Re =800 wall displacement and velocity are greater, vortex strength and size are lower, and vortex movement is enhanced. At this Re, the differences with the rigid case are more evident. A comparison of the velocity profiles of these two cases is presented in figure 40. Solid lines show profiles for a compliant model, while dotted lines correspond to the rigid case. An increase in diameter of the compliant wall (A) is accompanied by lower velocities when compared to the rigid. Velocities in the compliant model increase with an increase in the local Reynolds number (phase B), nut still lower than rigid case. The deceleration phase begins, the wall starts to contract, and velocities start to increase (D). The flow decelerates to near zero before it reverses at phase F. Up to phase G, flow is in the upward direction accelerating. Between G and I, flow disturbances are identified.

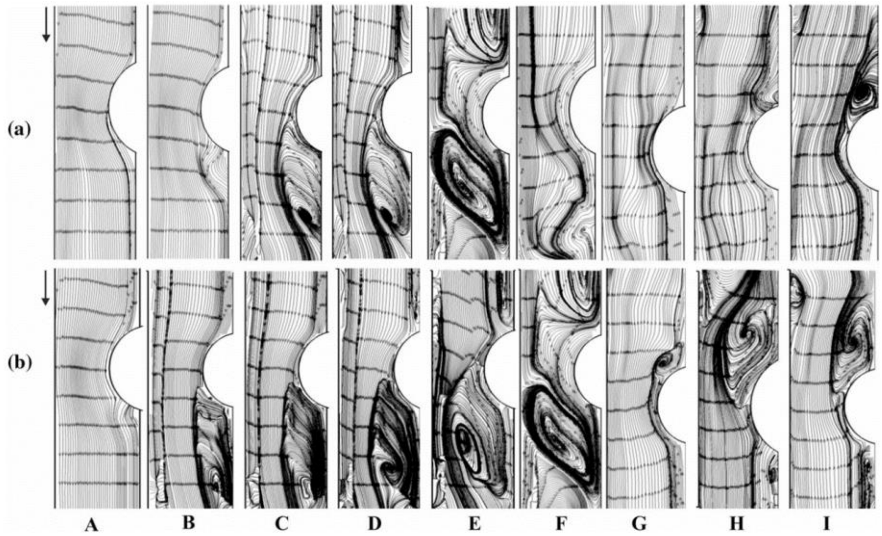

Figure 38: Stream traces during pulsatile flow in asymmetric rigid constriction at (a) Re=300 and (b) Re=800 [24]

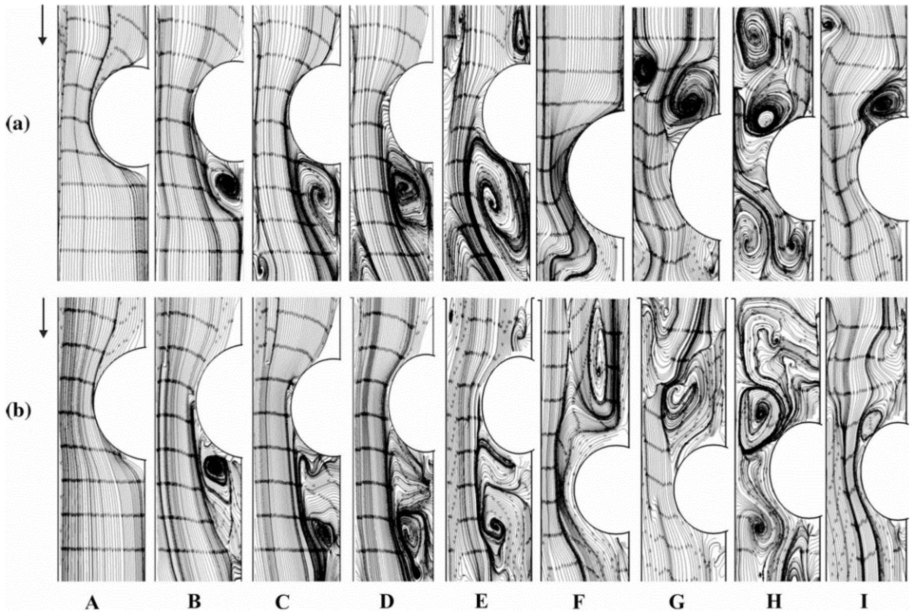

Figure 39: stream traces obtained during pulsatile flow in an asymmetric flexible constriction of 3 mm thickness; (a) Re=300, (b) Re=800 [24]

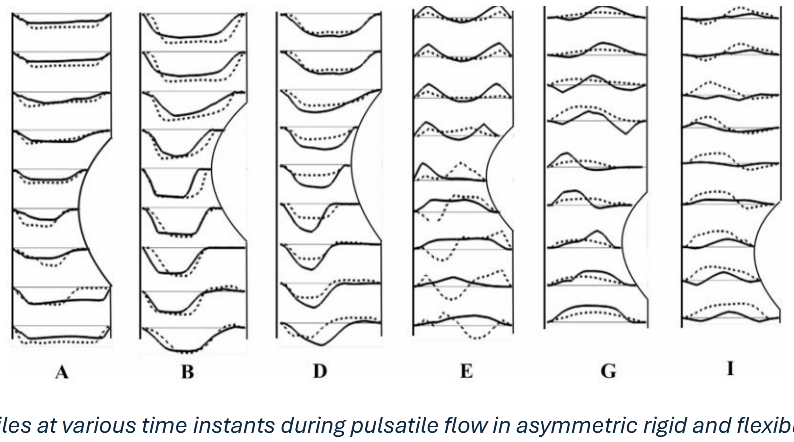

Figure 40: Velocity profiles at various time instants during pulsatile flow in asymmetric rigid and flexible constriction; Re =800 [24]

4.5 Roughness effects

Within the scope of aortic valve stenosis, in addition to the restriction in the flow due to an incomplete opening of the aortic valve, calcification of the aortic valve deforms the shape of its leaflets. This introduces roughness [36] on the surface of the walls bounding the flow. The bumpy and irregular nature of the leaflets changes the flow field and can enhance the turbulence and the fluctuations. The nature of the deformed surface can be investigated by the analysis of the spectral content of the sound signals captured from these flows. The sound signals themselves are not a direct measure of turbulence, but surface pressure is related to turbulence intensity, and the wall pressure fluctuations that gives rise to audible sounds are influenced by the core region of turbulent flows.

Roughness on the surface of a wall-bounded flow has an impact on the mean velocity profile and statistics. In a turbulent boundary layer, a mesh-type surface roughness decreases the magnitude of the streamwise velocity fluctuations while enhancing the wall-normal fluctuations and thus redistributing energy. The wall-normal component of fluctuations is reduced near the wall when the roughness elements are cylindrical in their shape. Except in the very near wall area, the pressure transport term does not have significant changes. The result of enhanced roughness in a physiologically relevant setting would indicate that the increase in drag within the system would require greater work to overcome the friction, regardless of the exact shape or nature of the roughness itself. The work of Byers et al. [36] investigates the influence of surface roughness through the changes in acoustic spectral content.

The acoustic spectrum shows which frequencies present contain greater amounts of energy. Higher order statistics are capable of defining new features that can be identified by signal analysis: one such measure is bicoherence. It provides a normalized measure of frequency coupling between two frequencies f_1 and f_2 in a flow. Bicoherence is a normalization of the bispectrum, where Fourier transform of a time varying signal and complex conjugate of the Fourier transform appear. Identification of frequencies of interest in the sound signal using bicoherence provides greater insight into which frequencies are a result of the modified geometry in the flow field.

Four different roughness scenarios are introduced, ranging from smooth to a relative roughness of 0.0486 based on the diameter. These span three different restriction severities ranging from moderate (56% restricted) to severe (82% restricted) based on the American Society of Echocardiography rating of aortic stenosis. The flow is driven with a ViVitro Labs 'superpump' pulsatile pump that operates at 1.17 Hz. The pulse shape is set to a waveform that mimics the pulse of a heart. Also, the geometry of the valve opening and the volume flow rate are similar to regular human heart conditions. Reynolds numbers match the ones encountered in most human heart conditions, corresponding to 5407, 6554, 8214 and 9831. Because large vessels are taken into account, blood flow is approximated with a Newtonian behaviour: it is thus possible to use water for the experiments. The roughness is introduced to the inner surface of the narrowing by utilizing sandpaper grit roughness elements and gluing with a thin general purpose cyanoacrylate glue. Note that when adding the roughness, a finite thickness is introduced to the walls, slightly increasing the overall restriction. The RMS sizes for each are 80 grit (ε = 0.250 mm), 100 grit (ε = 0.150 mm) and 120 grit (ε = 0.125 mm). Sound signals are acquired with a Biopac contact microphone placed over the restriction with the gain set to 200 and a low pass filter at 5 kHz and high pass filter at 0.05 Hz. For each experiment five independent one-minute trials were collected. In order to compare the different cases, a normalization is mandatory.

From the results, it is apparent that changing the severity of the restriction has a significant impact on the distribution of energy in the power spectrum (figure 41a). The forcing frequency and the first few harmonics are quite prominent: there are two prominent peaks of energy around 30 Hz and 100-200 Hz. For the highest restriction, the spectral shape has shifted significantly. For a given restriction and surface roughness, the distribution of energy remains consistent across all frequencies. The lower frequencies have broadly the same distribution of energy across all Reynolds numbers (figure 41b).

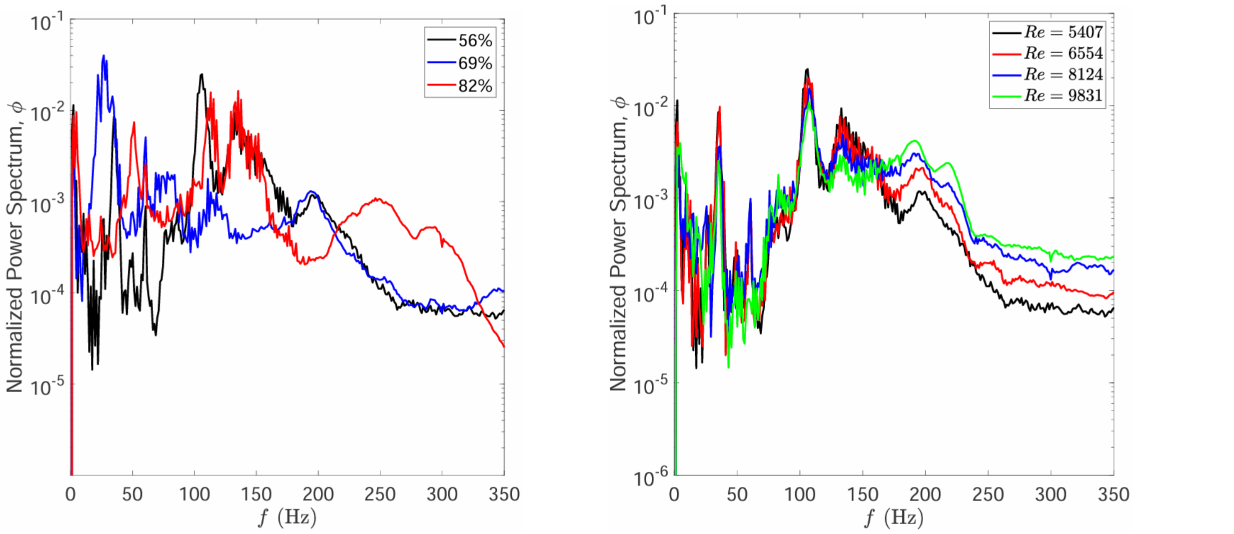

Figure 41: (a) Normalised power spectrum for fixed Re=5407, smooth case in 56%, 69% and 82% restrictions. (b) Normalised power spectrum for different Re in a smooth case for a 56% restriction [36]

Figure 42 shows a fixed restriction of 56%, a fixed Re=5407 and changing surface roughness. As the roughness changes, the spectral shape does not change. However, it appears that the roughness disrupts the low frequency regions and the higher frequencies, but a prominent peak at 100 Hz remains. The smallest of the three roughness elements (120 grit) enhances the relative energy content below 100 Hz in comparison to the smooth case. The two larger roughness elements more closely match the smooth case, with disruptions in the spectral shape at higher frequencies by a few Hz.

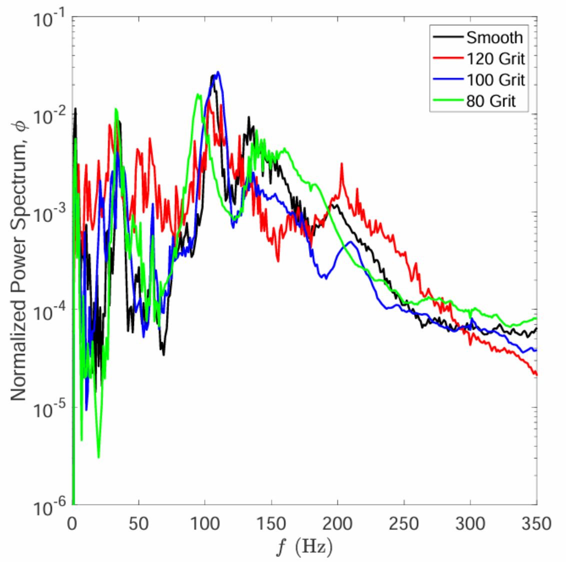

Figure 42: Normalised power spectrum for fixed Re and restriction, with changing roughness [36]

As roughness is introduced, the spectral content is altered, and in some cases drastically, still less than what happens with the introduction of restrictions. For the 56% restriction cases, the introduction of the smallest roughness element caused the spectrum to flatten out across all frequencies, with the prominent bands differing from the smooth 56%. As the relative roughness height is increased, the spectrum shifts back towards the baseline. A sensitive dependence on the geometry is thus evident. The effect of roughness at higher Reynolds number is less evident probably because of the larger flow rates.

4.6 Model of aortic stenosis (transition and turbulence)

In this section, the computational modelling and analysis of haemodynamics in a simple model of aortic stenosis by Zhu, Seo and Mittal [27] is reported, with particular focus on transitional and turbulence regimes. The study is motivated by considerations on heart murmurs and cardiac auscultations and is carried on through numerical simulations of a simple aorta with stenosis. The aorta is modelled as a curved pipe with a 180° turn, and three different stenoses with area reduction of 50%, 62.5% and 75% (figure 43) are discussed. A uniform steady inlet velocity with a Reynolds number of 2000 is used for all the cases. The post stenotic flow is dominated by the jet that originates from the stenosis as well as the secondary flow induced by the curvature: they both contribute significantly to the flow turbulence.

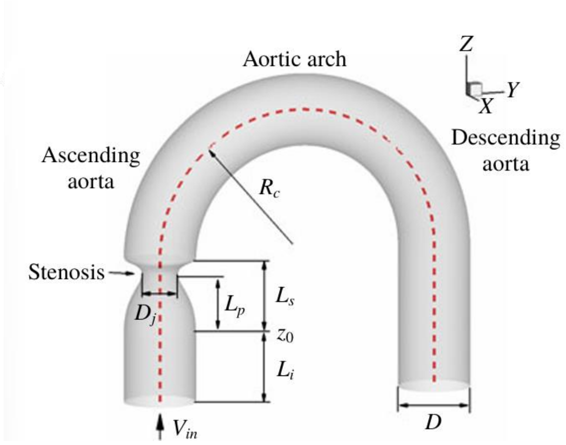

Figure 43: Schematic of the modelled aorta with an axisymmetric 75% stenosis. The dashed line represents the geometric centreline of the modelled aorta [27]

The studied flow lies in the transitional region, the transitional and turbulent characteristics will be now discussed. Figure 44a shows the turbulent kinetic energy (TKE) distribution at θ=60° for the case of 62.5% stenosis. The high-TKE region forms a bridge-like shape with two ends near the anterior and posterior surfaces of the aorta. In 44b and c, the TKE distribution is overlapped with the mean streamwise and azimuthal vorticity components in that location. The Dean vortices partially overlap with the two ends of the TKE distribution, indicating the contribution from stochastic fluctuations within the secondary flows to the TKE. The secondary flows wrap around the jet and force it into the shape of a crescent (figure 44c). It must be noted that this specific angle is where the periodic vortex shedding transitions into more stochastic flow behaviour, accounting for the high TKE.

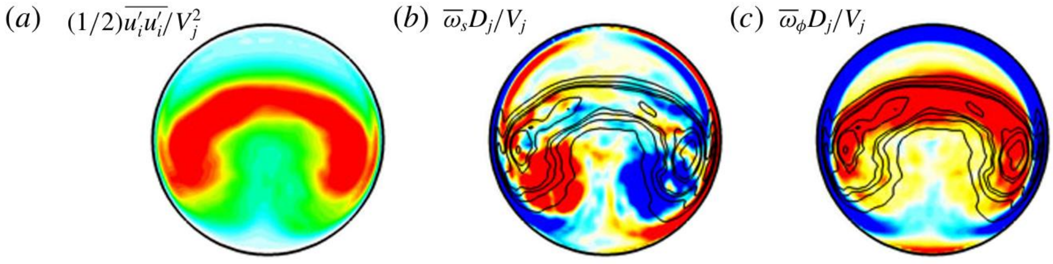

Figure 44: (a) TKE distribution, (b) TKE and streamwise vorticity, (c) TKE and mean azimuthal vorticity [27]

Figure 45 shows the spatial evolution of TKE for stenosis of 50%, 62.5% and 75%, plotted at different angles, to illustrate its spatial evolution. At the initial stage of the jet, the flow is still laminar, thus resulting in low TKE for θ<35°. It also stands out the fact that for 50% stenosis, vortex shedding is less intense: the TKE is not noticeable until θ=55°. It can also be observed that the high-TKE region moves closer to the outer wall and the anterior/posterior surface as the severity of the stenosis increases. It is worth mentioning that the TKE in figure 45 is non-dimensionalized by the mean jet velocity. If it were non-dimensionalized by the inlet velocity, the TKE intensity for 75% stenosis would appear to be much stronger than the other two under the same contour level.

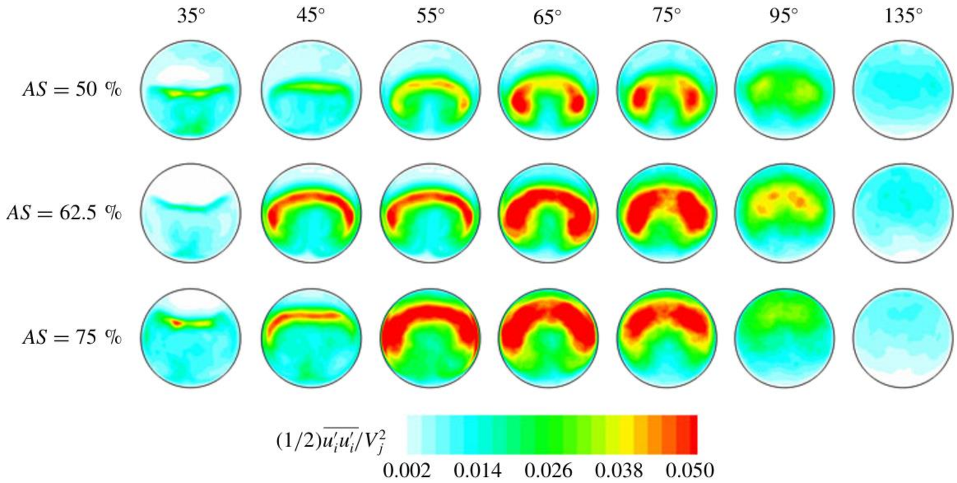

Figure 45: non-dimensionalized TKE for the three cases plotted at different angles, to illustrate its spatial evolution [27]

To sum up the results of this modelling, the turbulence is always preceded by the discrete-frequency vortex shedding. In the curved pipe model, the secondary flow induced by the curvature also contributes significantly to the total energy of turbulence. This is especially evident for the 50% stenosis, where the TKE resulting from the shear layer breakup is significantly lower than that from the secondary flow.

5. Conclusions

Transition from laminar to turbulent pulsatile flow has for long captured, and still does, the curiosity of fluid dynamicists, not only because it is a fascinating topic of unique mathematical challenge, but also because of its wide range of application in several fields, ranging from the industrial role to the medical sector. For what concerns the latter, a tight bond between some of the most common cardiovascular diseases and pulsatile flow turbulence exists. It is thus undeniable the importance of studying this type of flows and the benefits that can derive from the fully understanding of its mechanisms are numerous. Many aspects of the behaviour of pulsatile pipe flows are still under investigation and debate. A summary of the results discussed in the different chapters of this work is here reported.

From experimental evidence, for what concerns pulsatile flows in an ideal cylindrical pipe, it is possible to divide the transition to turbulence in three regimes, depending mainly on the Womersley number:
(i) for Wo>12 the transition threshold is unaffected by flow pulsation, as the rate changes are too fast for the turbulence to react.
(ii) for Wo<2.5 the changes of Re are slow enough to generate turbulent structures, whose survival is critical during the acceleration phases of the cycle.
(iii) in the intermediate region the transition thresholds vary between the two limits.

In the subcritical regime, two different types of turbulent structures can be observed: localized puffs and helical instabilities. The differences between these two are found in: the different amplitude that allows their generation, the direction of spreading and the triggering disturbances. In addition, helical instability depends on the presence of inflection points in the laminar flow. It is experimentally proved that the waveform of the pulsation has a direct influence on the characteristics of such points. For waveforms with longer low-velocity phases, the perturbations have more time to grow. Moreover, the more sudden are acceleration and deceleration, the higher are the changes for the perturbations to grow. Paradoxically, these waveform characteristics promote turbulence decay.
It is also found that the turbulent pulsatile flow has a beneficial effect for depletion efficiency, meaning that is more effective than a steady flow in the prevention of accumulation of trapped fluid in recirculating zones. Another characteristic is the delayed response of turbulence in the buffer layer, influencing the amplitude of the wall shear stress, that results lower than the laminar case.

For what concerns cardiovascular system, blood flow can be studied as a pulsatile pipe flow. Even if it's a non-Newtonian fluid, in most arteries it behaves like a Newtonian one. The cyclicity in cardiovascular system is given by the heart pumping cycle (systole and diastole). Considering blood flow in arteries as an example, different configurations can be analysed.
Constricted pipes, that can be found in the cardiovascular diseases of stenosis and atherosclerosis, are characterised by a vortex region post-constriction, that result in turbulence at a certain threshold. Constrictions also induce high shear stresses, flow separation and instabilities.
The vessels of the cardiovascular system ore most of the times not in a straight line, thus resulting in curved configurations. In curved pipes the centrifugal force due to curvature plays a role: for pulsatile flows it results in the formation of a pair of counter-rotating vortices, that affect velocity profiles. A secondary flow is observed, influencing turbulence intensity and energy dissipation.
Another characteristic of cardiovascular vessels is that their walls are not rigid, at least not if a person is in good health: this is the case of pipes with compliant walls. Non rigid walls lead to possible wall displacement, thus influencing flow pattern. Wall velocities energize the fluid and weaken vortex strength, resulting in a faster transportation of vortices.
Sometimes, it may happen that the aortic valve calcifies thus deforming the shape of its leaflets.

This brings surface roughness effects in the game. It is found that it has an impact on the mean velocity profile. In a turbulent layer, it decreases the magnitude of the streamwise velocity fluctuations and redistributes energy. Experiments show that roughness disrupts low frequency region and the high frequency one. In general, the introduction of roughness flattens the power spectrum curves.

For what concerns future developments in the study of pulsating pipe flow the trend is towards advanced numerical simulations to gain deeper insights into the complex, time-dependent behaviours of fluid dynamics under pulsating conditions. Numerical simulations, in particular those employing computational fluid dynamics and high-fidelity turbulence models, will play a crucial role in improving the understanding of the interaction of factors such as frequency, amplitude, and flow regime. Where experiments have difficulties in capturing some flow characteristics, such as transient phenomena and localized turbulent structures, numerical simulations allow a detailed analysis of them. On the other hand, numerical methods must be continually validated against experimental data to ensure accuracy. Regarding experimental techniques, improvements, such as the use of advanced non-invasive measurement tools (e.g., particle image velocimetry and laser Doppler anemometry), can enhance the precision and resolution of data collection. Nevertheless, experiments still face limitations such as high costs, complexity in capturing high-frequency pulsations, and difficulties in achieving ideal boundary conditions. As a consequence, a synergistic approach that combines both numerical simulations and experimental validations is essential for advancing the understanding and applications of pulsating pipe flow.

6. References

[1] D. Xu, S. Warnecke, B. Song, X. Ma, B. Hof, Transition to turbulence in pulsating pipe flow, J. Fluid Mech. 831, 418-432 (2017)

[2] R. Trip, D. J. Kuik, J. Westerweel, C. Poelma, An experimental study of transitional pulsatile pipe flow, Physics of Fluids 24, 014103 (2012)

[3] M. Avila, D. Barkley, B. Hof, Transition to Turbulence in pipe flow, Annual Review of Fluid Mechanics 55, 575-602 (2023)

[4] Stettler J. C., Hussain A. K. M., On transition of the pulsatile pipe flow, J. Fluid Mech., 170, 169-197 (1986)

[5] Yellin L., Laminar-turbulent transition process in pulsatile flow, Circulation Research, XIX (1966)

[6] I. J. Wygnanski, F. H. Champagne, On transition in a pipe. Part 1. The origin of puffs and slugs and the flow in a turbulent slug, J. Fluid Mech. 59, 281-335 (1973)

[7] W. H. Van Doorne, Westerweel J., The flow structure of a puff, Philosophical Transactions of the Royal Society, 367, 489-507 (2009)

[8] Moron D., Avila M., Turbulent puffs in transitional pulsatile pipe flow at moderate pulsation amplitudes, Physical Review Fluids, 9 (2), 024601 (2024)

[9] D. Xu, B. Song, M. Avila, Non-modal transient growth of disturbances in pulsatile and oscillatory pipe flows, Journal of Fluid Mechanics 907, R5 (2020)

[10] B. Pier, Peter J. Schmid, Optimal energy growth in pulsatile channel and pipe flows, Journal of Fluid Mechanics 926, A11 (2021)

[11] D. Feldmann, D. Moron, M. Avila, Spatiotemporal intermittency in pulsatile pipe flow, Entropy 23(1), 46, 1-19 (2021)

[12] D. Xu, M. Avila, The effect of pulsation frequency on transition in pulsatile pipe flow, J. Fluid Mech. 857, 937-951 (2018)

[13] B. Pier, Peter J. Schmid, Linear and nonlinear dynamics of pulsatile channel flow, Journal of Fluid Mechanics 815, 435-480 (2017)

[14] D. Xu, A. Varshney, X. Ma, B. Song, M. Riedl, M. Avila, B. Hof, Nonlinear hydrodynamic instability and turbulence in pulsatile flow, PNAS 117, 21, 11233-11239 (2020)

[15] C. H. Von Kerczek, The instability of oscillatory plane Poiseuille flow, J. Fluid Mech. 116, 91-114 (1982)

[16] D. Moron, D. Feldmann, M. Avila, Effect of waveform on turbulence transition in pulsatile pipe flow, Journal of Fluid Mechanics 948, A20 (2022)

[17] X. Liu, H. Zhu, Y. Bao, N. Srinil, D. Zhou, Z. Han, Time-delayed characteristics of turbulence in pulsatile pipe flow, Journal of Fluid Mechanics 979, A24 (2024)

[18] Arina R., Fondamenti di aerodinamica, Seconda edizione, Levrotto&Bella, Torino (2015)

[19] M. D. Jeronimo, D. E. Rival, On the lifespan of recirculating suspensions with pulsatile flow, Journal of Fluid Mechanics, 928, A2 (2021)

[20] H. Fujimoto, M. Kubo, T. Hama, H. Takuda, Transport Phenomena of Solid Particles in Pulsatile Pipe Flow, Hindawi Publishing Corporation, advances in Mechanical Engineering, 2010, 121326 (2010)

[21] David N. Ku, Blood flow in arteries, Annual Review of Fluid Mechanics 29, 399-434 (1997)

[22] Khanafer K., Berguer R., Fluid-structure interaction analysis of turbulent pulsatile flow within a layered aortic wall as related to aortic dissection, Journal of Biomechanics, 42 (16), 2642-2648 (2009)

[23] Jagos J., Kohut J., Skacel P., Bursa J., Influence of Turbulence in Aorta-like Tube: Computational and Experimental Study, Journal of Applied Fluid Mechanics 14 (5), 1411-1420, (2021)

[24] A. Y. Usmani, K. Muralidhar, Pulsatile flow in a compliant stenosed asymmetrical model, Experiments In Fluids, 57 (12), 186 (2016)

[25] R. Mittal, S.P. Simmons, F. Najjar, Numerical study of pulsatile flow in a constricted channel, Journal of Fluid Mechanics, 485, 337-378 (2003)

[26] N. Barrere, J. Brum, M. Anzibar, F. Rindeknecht, L.G. Sarasua, C. Cabeza, Lagrangian mixing of pulsatile flows in constricted tubes, Physics of Fluids 35, 021901 (2023)

[27] C. Zhu, J. H. Seo, R. Mittal, Computational modelling and analysis of haemodynamics in a simple model of aortic stenosis, Journal of Fluid Mechanics, 851, 23-49 (2018)

[28] Jahangiri M., Saghafian M., Sadeghi M. R., Numerical study of turbulent pulsatile blood flow through stenosed artery using fluid-solid interaction, Computational and Mathematical Methods in Medicine, 2015, 515613 (2015)

[29] Ding G., Choi K., Ma B., Kato T., Yuan W., Transitional pulsatile flows with stenosis in a two-dimensional channel, Physics of Fluids, 33 (3), 034115 (2021)

[30] A. Khair, A. Hossain, B. C. Wang, D. Kuhn, M. Molla, Direct numerical simulation of physiological pulsatile flow through a stenotic channel, Proceedings of the International Symposium on Turbulence, Heat and Mass Transfer, 2012, 1226-1238 (2012)

[31] M. D. Jeronimo, D. E. Rival, Particle Residence Time in pulsatile post-stenotic flow, Physics of Fluids, Volume 32 (4), 045110 (2020)

[32] M. D. Jeronimo, K. Zhang, D. E. Rival, Direct Lagrangian measurements of particle residence time, Experiments in Fluids, 60 (4), 72 (2019)

[33] Kalpakli Vester A., Orlu R., Alfredsson P.H., Turbulent flows in curved pipes: Recent advances in experiments and simulations, Applied Mechanics Reviews, 68 (5), 050802 (2016)

[34] Cai J., Hu M., Chen C., Babenko A., Xu Z., Shiju E., Numerical study of the pulsatile flow and aeroacoustics of straight and curved pipes, Numerical Heat Transfer; Part A: Applications, 85 (12), 1903-1921 (2024)

[35] J. Kuehnen, P. Braunshier, M. Schwegel, H. C. Kuhlmann, B. Hof, Subcritical versus supercritical transition to turbulence in curved pipes, Journal of Fluid Mechanics 770, R3 (2015)

[36] Clayton P. Byers, S. Ofori, L. Chapata, T. Ning, Non-linear measurements of roughness effects in pulsing restricted flows, ASME IMECE 9, 197186 (2023)

[37] P. K. Mandal, S. Chakravarty, A. Mandal, Numerical study of the unsteady flow of non-Newtonian fluid through differently shaped arterial stenoses, International Journal of Computer Mathematics, 84 (7), 1059-1077 (2007)

[38] Hidesato Ito, Flow in Curved Pipes, JSME International Journal, 30 (262), 543-552 (1987)

Ringraziamenti

Giunta alla fine di questi quasi tre anni vorrei ritagliare questo spazio per ringraziare chi è stato al mio fianco in questo percorso, anche se sono consapevole che le parole non saranno mai abbastanza.

Ringrazio la mia relatrice, la Prof.ssa Scarsoglio, per la disponibilità e per l'opportunità di lavorare a questa tesi.

Ringrazio i miei genitori, Mimma e Angelo, che ci sono sempre stati e il cui sostegno è sempre stata una certezza. Vi ringrazio perché non mi avete fatto mai mancare nulla e perché credete in me molto più di quanto faccia io. Grazie per sempre.

Ringrazio la mia squadra, i miei fratelli, i miei migliori amici, Emilio, Claudio e Beatrice. Ormai siamo avviati per le nostre strade, ci sentiamo poco e ci vediamo ancora meno, ma la consapevolezza che posso contare su di voi in ogni momento mi dà forza. Grazie.

Ringrazio le mie amiche di sempre, Chiara e Cristina, che mi hanno sempre supportato, che mi hanno insegnato cos'è l'amicizia, che basta poco per essere felici, che basta un sorriso a migliorare una giornataccia. Grazie per tutti i preziosi momenti insieme.

Ringrazio Alessandro, che è sempre stato per me un punto di riferimento, oltreché un sincero amico su cui contare, soprattutto negli ultimi anni. Grazie per la tua gioia contagiante.

Ringrazio i miei colleghi di università, nonché amici di vita, Edoardo e Nella, con cui ho condiviso la maggior parte delle giornate passate al Poli. Grazie, perché siete persone meravigliose e avete alleggerito questo percorso tra una sciata e l'altra.

Ringrazio tutti gli altri amici, che mi hanno accompagnato in questo percorso e che senza i quali non sarebbe stato lo stesso.

Grazie a tutti. Grazie per sempre.